Title

First-Principles Simulation of Carrier Recombination Mechanisms in Halide Perovskites

Journal

ADVANCED ENERGY MATERIALS, 10(13)

ISSN

1614-6832

Authors

Zhang, Xie

Shen, Jimmy-Xuan

Van de Walle, Chris G

Publication Date

2020

DOI

10.1002/aenm.201902830

Peer reviewed

WILEY-VCH

DOI:
Article type: Progress Reports

Title First-principles simulation of carrier recombination mechanisms in halide perovskites

Xie Zhang[†,*], *Jimmy-Xuan Shen*[†,*], *and Chris G. Van de Walle*[*]

† These two authors contributed equally to this work.
Dr. X. Zhang, Prof. C. G. Van de Walle
Materials Department, University of California, Santa Barbara, CA 93106-5050, USA
E-mail: xiezhang@ucsb.edu
E-mail: vandewalle@mrl.ucsb.edu
Dr. J.-X. Shen
Department of Physics, University of California, Santa Barbara, CA 93106-9530, USA
Present address: Department of Materials Science and Engineering, University of California, Berkeley, CA 94720, USA
E-mail: jmmshn@lbl.gov

Keywords: First principles, radiative recombination, Auger recombination, halide perovskites

In recent years we have seen remarkable developments in halide perovskites, which are used in highly efficient optoelectronic devices and exhibit intriguing materials physics. Detailed knowledge of carrier recombination mechanisms is essential for understanding their excellent performance and to further increase their efficiency. Obtain such knowledge is challenging, however, and different studies have reached divergent conclusions in some cases. This Progress Report outlines the critical developments in understanding the carrier recombination mechanisms in halide perovskites from a computational perspective. We focus on radiative and Auger recombination, since they have not been systematically assessed and discussed before, and a number of important issues have been actively debated. Our comprehensive discussion of the carrier recombination mechanisms is aimed at establishing physically justified insights that can form the basis for better materials and devices design.

1. Introduction

Halide perovskites are a class of materials that crystallize in the perovskite structure with a

chemical formula ABX_3, where the X sites are occupied by halogen atoms (Cl, Br and I). **Figure 1a** depicts the typical chemical compositions[1] of halide perovskites. Hybrid perovskites are a subgroup of halide perovskites; in the hybrid perovskites an organic molecule sits on the A site, surrounded by corner-shared B-X octahedra. **Figure 1b-d** shows the crystal structures of three different phases of a prototypical hybrid perovskite, $MAPbI_3$ (MA = CH_3NH_3), which undergoes phase transformations from cubic to tetragonal at T = 327 K and from tetragonal to orthorhombic at T = 162 K during cooling[2]. The crystal structures of the three phases differ by rotation of the inorganic octahedral cages. Even though these materials have been known for a long time[3,4], they only started receiving significant attention after they were considered for solar-cell applications in 2009[5]. Starting from a power conversion efficiency of 3.8% in the first photovoltaic demonstration[5], reported efficiencies have been constantly increasing[6–12] and the latest certified record has exceeded 23%[13]. Besides the high efficiencies, another advantage of halide perovskites is that they can be easily and cheaply fabricated[14], making them very attractive for next-generation solar cells. However, they do have drawbacks. Two major issues that are actively being studied[15,16] are their chemical, structural, thermal, and photo instabilities[17–21], and toxicity due to the presence of Pb[22]. Buoyed by the impressive success in photovoltaics, the application spectrum of halide perovskites has been extended to other technologically important devices such as light-emitting diodes (LEDs)[23], lasers[24], photocatalysts[25], actuators[26], and scintillators[27].

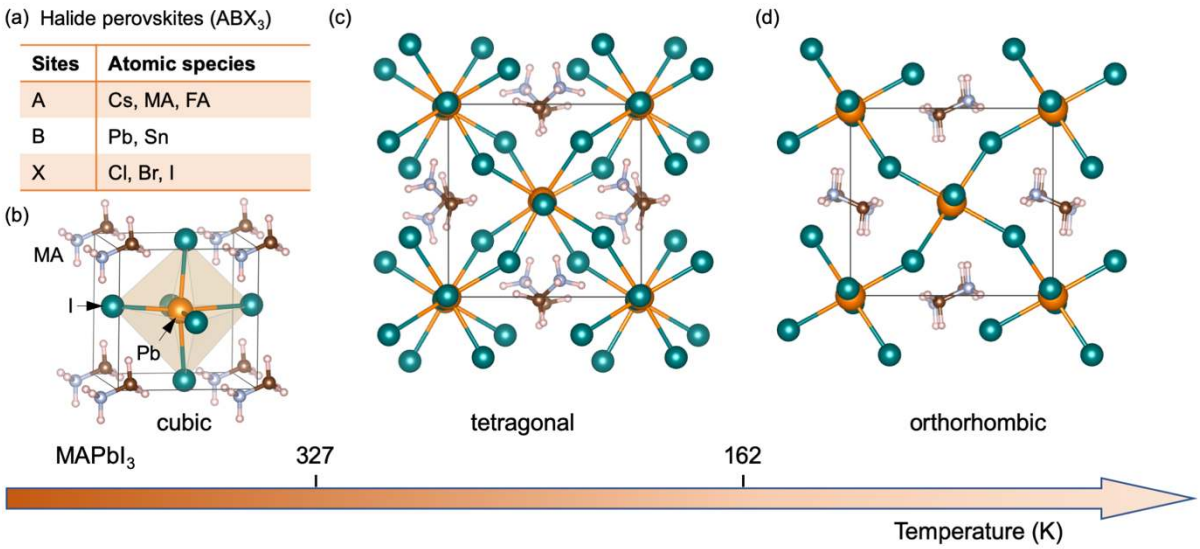

Figure 1. a) Typical chemical compositions of halide perovskites. MA stands for methylammonium (CH_3NH_3) and FA refers to formamidinium [$HC(NH_2)_2$]. b-d) Crystal structures of $MAPbI_3$ in the cubic b), tetragonal c) and orthorhombic d) phases. The critical temperatures of the phase transitions are marked on the temperature axis.

Understanding the origin of the high conversion efficiency has been a key topic of halide-perovskite research[28–38]. From a quantum-mechanical point of view, the efficiency is determined by the carrier recombination processes. As shown in **Figure 2**, the three main carrier recombination processes are the first-order defect-assisted Shockley-Read-Hall (SRH) recombination, the second-order radiative recombination, and the third-order Auger recombination. For the SRH recombination, electrons and holes recombine via deep-level defects in the band gap and the energy released by electron-hole recombination gets dissipated to phonons (**Figure 2a**). In radiative recombination, electrons and holes directly recombine and emit photons (**Figure 2b**), which is the desired light-emitting mechanism in an LED. Auger recombination is comprised of two types of processes: when an electron and a hole recombine, the excess energy and momentum can be captured by a third carrier, which gets promoted to a higher-lying state; If the third carrier is an electron, the Auger recombination is an electron-electron-hole (eeh) process (**Figure 2c**), otherwise it is a hole-hole-electron (hhe) process (**Figure 2d**). The coefficients of the three recombination channels determine the evolution of carrier density n with time t, as expressed in the rate equation:

$$\frac{dn}{dt} = -An - Bn^2 - Cn^3, \quad (1)$$

where A, B, and C are the coefficients describing SRH, radiative and Auger recombination, respectively. These coefficients ultimately determine the efficiency of the devices.

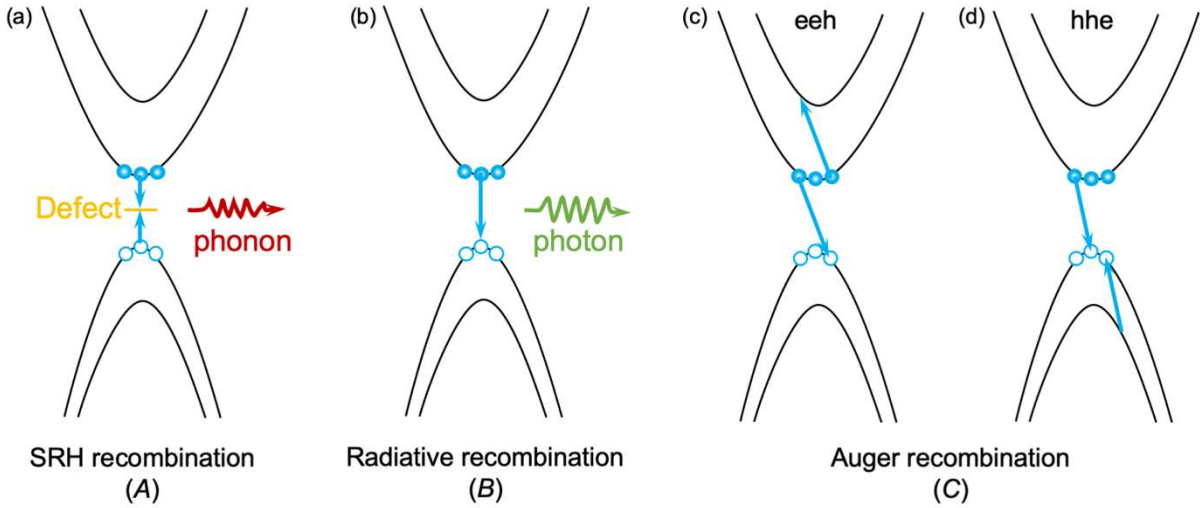

Figure 2. Schematic illustration of different recombination processes: a) Shockley-Read-Hall (SRH) recombination, b) Radiative recombination, and c,d) Auger recombination including electron-electron-hole (eeh) and hole-hole-electron (hhe) processes. The light-blue solid and open spheres denote electrons and holes, respectively. A, B and C are the corresponding recombination coefficients.

A number of experimental techniques can be used to determine recombination rates, such as transient spectroscopy[39–41] and photoluminescence[42–44]. The central idea is to fit, e.g., photoluminescence decay data at different incident fluences to Equation (1). There are several major challenges for such experiments[42,45]: i) the key variable, namely the carrier density is not directly known—it is often indirectly determined by assuming a constant photon-to-carrier conversion ratio of 1; ii) the simultaneous fit of three recombination coefficients can introduce large uncertainties; and iii) additional processes that are not included in the standard rate equation, such as escape of carriers from the recombination region, may affect the observed rate. These challenges may explain why reported recombination coefficients from different sources often differ by several orders of magnitude[46].

Even if accurate recombination coefficients are obtained, they do not in themselves identify the

underlying recombination mechanisms. For instance, the presence of a third-order process may be due to Auger recombination, but could also reflect other processes such as carrier leakage, as illustrated by investigations on the much more intensively studied nitride semiconductors[47]. The problems associated with interpretation of experimental measurements highlight why first-principles calculations of carrier recombination coefficients are particularly valuable. In recent years there have been remarkable developments in the first-principles methodology for calculating carrier recombination coefficients[48–52]. Some of them have already been applied to halide perovskites[53–59], producing a number of important insights.

The aim of the present progress report is to outline the state-of-the-art first-principles methodology for calculating carrier recombination coefficients and the critical insights that have been achieved for halide perovskites. Since first-principles calculations of defects in halide perovskites and their role in SRH recombination have been discussed in other reviews[60–62], we focus on radiative and Auger recombination in the present report. This report is organized as follows: We first briefly review the first-principles methodology for simulating carrier recombination in Section 2. In Section 3, we discuss the important questions and insights for the radiative recombination in halide perovskites. A special focus is placed on the Rashba effect, which refers to changes in the band structure induced by spin-orbit coupling (SOC) in materials that lack inversion symmetry. In Section 4, we present the latest progress regarding Auger recombination mechanisms in halide perovskites and potential avenues for overcoming the fundamental bottleneck through band-structure engineering. Finally, in Section 5 we summarize the key findings and provide an outlook for the future research efforts on carrier recombination mechanisms in halide perovskites.

2. First-principles methodology

The basic theory for computing recombination coefficients has been discussed in detail in a number of book chapters and methodological articles[52,63,64]; we refer the reader to these

references for detailed derivations. Our aim here is to provide an overview of the formalism for and to describe how recombination coefficients can be practically evaluated in the context of first-principles electronic-structure calculations. As mentioned above, we focus on radiative and Auger recombination. For defect-assisted SRH recombination, we refer the reader to methodological articles such as Ref.[50].

2.1. Radiative recombination

Since SOC is strong in halide perovskites and since the corresponding spin texture has been suggested to significantly impact radiative recombination, we first present a first-principles approach to calculating the spin texture of electrons and holes and then describe how to compute radiative recombination coefficients from first principles.

The three components of the spin operators are given by the Pauli matrices.

$$\hat{S}_x = \begin{pmatrix} 0 & 1 \\ 1 & 0 \end{pmatrix}, \hat{S}_y = \begin{pmatrix} 0 & -\mathrm{i} \\ \mathrm{i} & 0 \end{pmatrix}, \hat{S}_z = \begin{pmatrix} 1 & 0 \\ 0 & -1 \end{pmatrix}. \tag{2}$$

The expectation values of the each component of spinor can be evaluated by[55]

$$S_x(i,\mathbf{k}) = \langle \psi^*_{i,\mathbf{k}} | \hat{S}_x | \psi_{i,\mathbf{k}} \rangle , \tag{3}$$

$$S_y(i,\mathbf{k}) = \langle \psi^*_{i,\mathbf{k}} | \hat{S}_y | \psi_{i,\mathbf{k}} \rangle , \tag{4}$$

$$S_z(i,\mathbf{k}) = \langle \psi^*_{i,\mathbf{k}} | \hat{S}_z | \psi_{i,\mathbf{k}} \rangle , \tag{5}$$

where $\psi_{i,\mathbf{k}}$ is the wave function of the i^{th} band at the reciprocal lattice vector $\mathbf{k}$, which can be calculated using standard first-principles codes such as the Vienna *Ab initio* Simulation Package (VASP)[65] and Quantum Espresso[66].

Assuming a charge-neutral system the radiative recombination coefficient (B) can be determined based on Fermi's golden rule[56]:

$$B = \frac{n_{\mathrm{r}} e^2}{\pi \epsilon_0 m_{\mathrm{e}}^2 c^3 \hbar^2 n^2 V} \sum_{\mathbf{cvk}} f_{\mathbf{ck}}(1 - f_{\mathbf{vk}})(\varepsilon_{\mathbf{ck}} - \varepsilon_{\mathbf{vk}}) \, |M_{\mathbf{cvk}}|^2 , \tag{6}$$

where n_{r} is the refractive index, e the elementary charge, m_{e} the free electron mass, ϵ_0 the vacuum permittivity, c the speed of light and $\hbar$ the Planck constant. n is the carrier density and

V the volume of a unit cell. $f_{\mathbf{ck}}$ is the Fermi occupation factor for an electron in the conduction band c at momentum **k**, which is given by

$$f_{\mathbf{ck}} = \frac{1}{1+e^{\frac{\varepsilon_{\mathbf{ck}}-\mu_{\mathrm{c}}}{k_{\mathrm{B}}T}}}, \tag{7}$$

where $\varepsilon_{\mathbf{ck}}$ is the eigenvalue of the electron state c at **k**. μ_{c} is the quasi-Fermi level of electrons, k_{B} is the Boltzmann constant, and T the absolute temperature. Similarly, we have the Fermi occupation factor for a hole in the valence band v at **k**:

$$f_{\mathbf{vk}} = \frac{1}{1+e^{\frac{\varepsilon_{\mathbf{vk}}-\mu_{\mathrm{v}}}{k_{\mathrm{B}}T}}}. \tag{8}$$

Since the occupation of electrons (and holes) should sum up to the total number of carriers in the cell with volume V, we have the following relation:

$$\sum_{\mathbf{ck}} f_{\mathbf{ck}} = \sum_{\mathbf{vk}} (1 - f_{\mathbf{vk}}) = n N_{\mathbf{k}} V, \tag{9}$$

where $N_{\mathbf{k}}$ is the total number of **k** points used for sampling the Brillouin zone. In practice, we start from a given carrier concentration n and solve Equation (9) (using, e.g., a bisectioning approach) to obtain the quasi-Fermi levels for electrons and holes, and thus the Fermi occupation factors for all states.

$M_{\mathrm{cv}\mathbf{k}}$ is the momentum matrix element between a conduction band state c and a valence band state v at **k**, averaged over the three components (p_{x}, p_{y} and p_{z}) of the momentum operator[67].

$$|M_{\mathbf{cvk}}|^2 = \frac{1}{3}\sum_i |\langle \psi_{\mathrm{c}} | p_i | \psi_{\mathrm{v}} \rangle|^2, \tag{10}$$

where $i = x$, y, and z. ψ_{c} and ψ_{v} are the wave functions of the conduction band c and valence band v, respectively.

All of the above parameters and variables required can be obtained from first-principles electronic-structure calculations. To obtain a well-converged radiative recombination coefficient, one needs to sample the Brillouin zone with a very dense **k**-point grid. This can be achieved by performing a self-consistent electronic-structure calculation on a coarse **k**-point grid, followed by non-self-consistent calculations for every **k** point on a dense grid (e.g., 50 × 50 × 50) or by Wannier interpolations[68].

2.2. Auger recombination

Similar to the computation of radiative recombination coefficient, the Auger coefficient (*C*) of a charge-neutral system can also be described using Fermi's golden rule[57]:

$$C = \frac{2\pi}{\hbar n^3}\sum_{\mathbf{1234}} f_{\mathbf{1}} f_{\mathbf{2}}(1-f_{\mathbf{3}})(1-f_{\mathbf{4}})|M_{\mathbf{1234}}|^2\delta(\varepsilon_{\mathbf{1}}+\varepsilon_{\mathbf{2}}-\varepsilon_{\mathbf{3}}-\varepsilon_{\mathbf{4}}) , \qquad (11)$$

where the four single-particle states involved in an Auger process are labelled as **1**, **2**, **3**, and **4**. f_i (i = **1**, **2**, **3**, **4**) are the Fermi occupation factors, which can be determined in the same way as in the radiative recombination calculation. Energy conservation is guaranteed by the δ function. $M_{\mathbf{1234}}$ is the screened-Coulomb matrix element that includes two types of processes: direct ($M^{\mathrm{d}}_{\mathbf{1234}}$) and exchange ($M^{\mathrm{x}}_{\mathbf{1234}}$). When spin is taken into account, it can be derived as[52]

$$|M_{\mathbf{1234}}|^2 = \left|M^{\mathrm{d}}_{\mathbf{1234}} - M^{\mathrm{x}}_{\mathbf{1234}}\right|^2 = |\langle\psi_{\mathbf{1}}\psi_{\mathbf{2}}|W|\psi_{\mathbf{3}}\psi_{\mathbf{4}}\rangle - \langle\psi_{\mathbf{1}}\psi_{\mathbf{2}}|W|\psi_{\mathbf{4}}\psi_{\mathbf{3}}\rangle|^2 , \qquad (12)$$

where ψ_i (i = **1**, **2**, **3**, **4**) are the wave functions of the four states involved in an Auger process. W is the screened Coulomb interaction, which can be represented as a reciprocal-space sum[52]

$$W(\boldsymbol{r}_1,\boldsymbol{r}_2) = \frac{1}{V}\sum_q \frac{1}{\epsilon(\mathbf{q})}\frac{4\pi e^2}{\mathbf{q}^2+\lambda^2} e^{\mathrm{i}\mathbf{q}(\boldsymbol{r}_1-\boldsymbol{r}_2)} , \qquad (13)$$

where $\boldsymbol{r}_1$ and $\boldsymbol{r}_2$ are the spatial locations of two carriers and V the cell volume. $\epsilon(\mathbf{q})$ is the static dielectric function, which is determined by using a model dielectric function[69]. λ is the inverse screening length due to free carriers.

In practice, one searches for all possible combinations of four states among different bands on a dense discrete **k**-point grid that satisfy momentum conservation (i.e., $\mathbf{k_1} + \mathbf{k_2} = \mathbf{k_3} + \mathbf{k_4}$), and evaluates the matrix elements for each one of them. By summing over the contributions from all of the combinations that are identified, one obtains the total Auger coefficients for the eeh (C_n) and hhe (C_p) processes.

3. Radiative recombination

One of the features of halide perovskites that has often been invoked to explain the high power conversion efficiency is the long carrier lifetime, typically on the order of 100 ns[70]. For a long time, this was attributed to slow radiative recombination due to the presence of strong Rashba effect in these materials[31,33,71,72]. While a number of experimental studies have been performed to measure the recombination coefficients, conclusive statements cannot be made based solely on experimental data since the experimentally reported radiative recombination coefficients vary by more than three orders of magnitude[40,42,45,46,59,73–75]. Computational studies based on model theories[31,71] argued that the radiative recombination in $MAPbI_3$ is spin-forbidden or strongly suppressed by the Rashba-induced momentum splitting at the band edges, thus further strengthening the belief that slow radiative recombination in halide perovskites is responsible for the observed long lifetimes and triggering additional follow-up studies[33,72,76–79]. Only when rigorous first-principles calculations for the spin texture and radiative recombination coefficient were performed did it become clear that radiative recombination is actually strong in halide perovskites, with a magnitude comparable to conventional direct-gap semiconductors such as GaAs. In this section, we discuss the recent progress in understanding the Rashba effect and its impact on the radiative recombination in halide perovskites, in the process clearing up some misunderstandings in the field and providing a transparent physical picture for the radiative recombination process in halide perovskites.

3.1. The Rashba effect

The combination of a lack of inversion symmetry with strong SOC leads to a linear momentum splitting in the band structure (see **Figure 3a**), commonly referred to as the Rashba effect[80,81]. The Rashba effect splits spin-degenerate bands by shifting their extrema away from the high-symmetry **k** point in opposite directions. If only the conduction-band minimum (CBM) or the valence-band maximum (VBM) splits, or if both split but by different amounts, then the material will have a slightly indirect band gap since the band extrema will exhibit a momentum mismatch. Another important consequence of the Rashba effect is that the orientations of the electron and hole spins at the band edges may form different patterns, the so-called spin texture. In the case of Rashba, the spin texture is characterized by a helical pattern[81] as shown in **Figure 3b**. Another type of spin texture, illustrated in **Figure 3c**, is named after Dresselhaus[81,82].

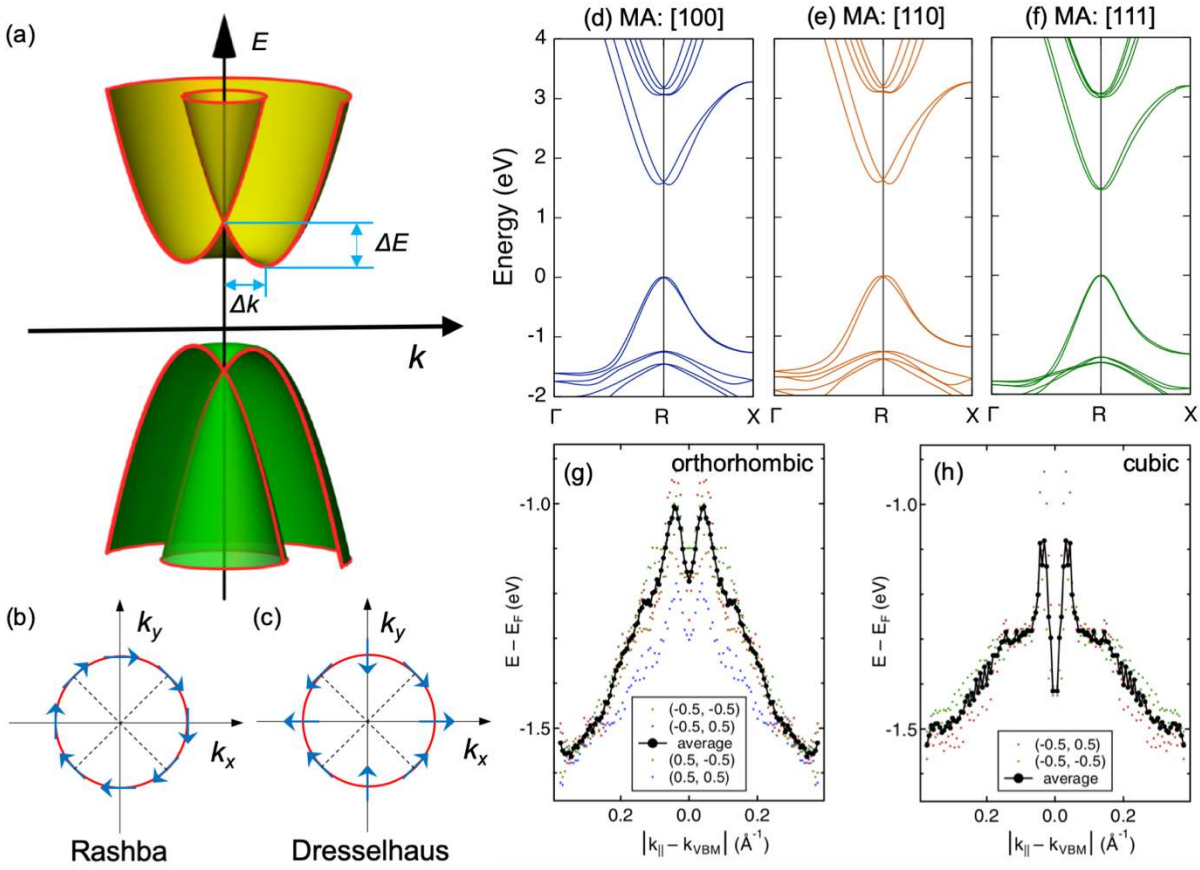

Figure 3. a) Schematic illustration of the Rashba effect with momentum splitting Δk and energy splitting ΔE. Adapted with permission[56]. Copyright 2018, American Chemical Society. b) Rashba-type spin texture. c) Dresselhaus-type spin texture. d-f) The band structure of $MAPbI_3$ with MA oriented along the [100], [110], and [111] directions, respectively, calculated using first principles including the SOC effect. g,h) The ARPES-measured band dispersions after

azimuthal averaging for the orthorhombic and cubic phases of $MAPbBr_3$, respectively. The dots of different colors correspond to different high-symmetry directions. The black lines depict the average. Adapted with permission[83]. Copyright 2016, American Physical Society.

In the case of $MAPbI_3$, even though we constrain the unit cell to have a cubic shape, the presence of the dipolar MA cation breaks the inversion symmetry. Pb and I are heavy elements, leading to strong SOC. The combination of inversion asymmetry and strong SOC leads to significant Rashba splitting. Since the energy barrier for the MA molecule to rotate inside the inorganic Pb-I lattice is only around 20 meV[84], at room temperature the MA molecule can already rotate easily, which results in a dynamic crystal structure and also a dynamic Rashba effect[85,86]. **Figure 3d-f** shows the band structure of $MAPbI_3$ with MA oriented along three high-symmetry directions: [100], [110], and [111], calculated from first principles using the Heyd-Scuseria-Ernzerhof (HSE)[87] functional and including the SOC effect. It can be seen that for the [111] orientation the Rashba splitting is negligibly small, while it is much more pronounced for the [100] and [110] orientations. We can understand this as follows. The MA molecule impacts the band edges through distorting the Pb-I sublattice. The CBM is composed primarily of Pb *p* states, while the VBM is primarily composed of I *p* states. When MA is oriented along [111], the Pb and I atoms are close to their ideal perovskite positions, leading to negligible Rashba splitting. But if MA is oriented along [110], the Pb-I sublattice is maximally distorted, which results in the largest Rashba splitting. Due to the difference in the orbital characters, the momentum splitting at the CBM is larger than the one at the VBM.

Niesner et al. measured the valence-band dispersion of $MAPbBr_3$ using angle-resolved photoelectron spectroscopy (ARPES)[83] and reported that the SOC strength of $MAPbBr_3$ is among the largest ever observed. As shown in **Figure 3g,h**, both for the low-temperature orthorhombic phase and the room-temperature cubic phase, pronounced momentum splitting in the vicinity of the VBM is observed. The magnitude of the energy dispersion reported by Niesner et al.[83] is larger than our calculated value; in addition to the difference in the halogen

species (Br versus I), this could be due to surface effects, as noted by Frohna et al.[88] Since ARPRES can only characterize occupied bands, experimentally the splitting at the CBM is not yet clear.

These theoretical and experimental results indicate that a strong Rashba effect is present. However, the strong Rashba effect itself does not necessarily imply a significant suppression of radiative recombination. The exact impact of the Rashba effect depends sensitively on the relative spin orientation and momentum mismatch between states in the vicinity of the CBM and VBM, which we now discuss in detail in Sections 3.2 and 3.3.

3.2. Rashba spin splitting

Because of the Rashba effect, the bands in each split pair have opposite spin orientations. In halide perovskites, both the conduction and valence bands split. The band edges all have helical-type spin texture, and the relative spin orientations between the band edges are key for recombination processes. Based on a phenomenological Rashba effective model[89], Zheng et al.[31] found that the band edges have opposite spin orientations in $MAPbI_3$ (as schematically shown in **Figure 4a**): in the conduction bands, the inner branch has clockwise spin while the outer branch has counter-clockwise spin. For the valence bands, the spin orientations of both the inner and outer branches are exactly opposite to those of the corresponding conduction bands. Due to the different spin orientations between the band edges, Zheng et al. concluded that the radiative recombination in $MAPbI_3$ is spin-forbidden.

However, the spin texture produced by the Rashba effective model[31] is incorrect. The problem with this model, as applied by Zheng et al.[31], is that it imposes the same constant perturbation on the conduction and valence bands. This produces a helical spin texture, but (since the effective mass of holes has the opposite sign of electrons) the induced momentum splitting shifts the VBM and CBM toward opposite directions in momentum. This results in band edges

that always have mismatched spins. Zheng et al. [31] actually acknowledged that different perturbations can be applied to each of the band edges by projecting the Hamiltonian onto separate Hamiltonians for the valence band and the conduction band. Changing the magnitude of the perturbation then represents different strength of Rashba splitting for valence versus conduction band, but to capture the correct spin orientation also the *sign* of the perturbation should be reversed.

We performed first-principles calculations of the spin texture in $MAPbI_3$[55] using the methodology presented in Section 2.1. As schematically illustrated in **Figure 4b**, the first-principles result leads to a conclusion opposite to that of Zheng et al.[31]: the band edges have the *same* spin orientation and consequently the radiative recombination between the band edges is spin-allowed. **Figure 4c** presents the first-principles band structure of $MAPbI_3$ using the HSE[87] hybrid functional with the SOC effect included. In this calculation, the MA molecule is oriented along [100]. Large Rashba splitting in the conduction bands and relatively small splitting in the valence bands are evident. **Figure 4d-g** depicts the spin texture of the inner and outer branches for both the conduction and valence bands. In these figures, the two-dimensional arrows represent the (S_x, S_y) components of the spinors, while the third component (S_z) is visualized by the background color. A close inspection of these results revealed two important insights.

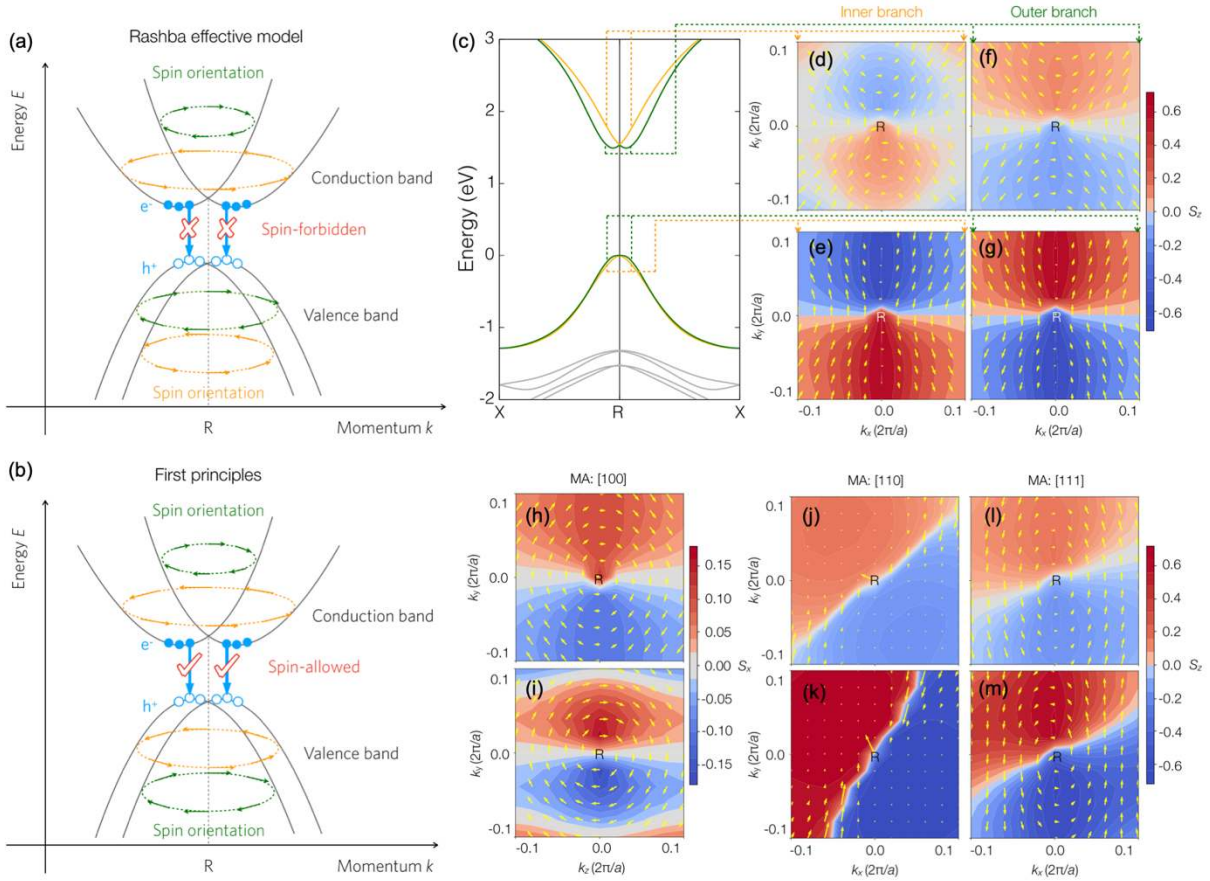

Figure 4. a) Schematic of the spin-forbidden transition based on a phenomenological Rashba effective model. b) Schematic of the spin-allowed transition based on first-principles calculations. c) First-principles band structure of $MAPbI_3$ using the HSE hybrid functional including SOC with the MA molecule oriented along [100]. d-g) The explicitly calculated spin texture of the inner and outer branches of the band edges, plotted in a (001) plane. h,i) The spin texture of the outer branches of the band edges, plotted in a (100) plane. j-m) The calculated spin texture of $MAPbI_3$ with the MA molecule oriented along [110] and [111]. Adapted with permission[55]. Copyright 2018, American Chemical Society.

First, the band edges have consistent spin orientation, indicating spin-allowed radiative recombination. Second, the spin texture does not reflect the Rashba-type helical pattern, but is consistent with rotating the standard Dresselhaus-type[82] spin texture (see **Figure 3c**) by 45°. We found that the exact pattern of the spin texture relates to the internal polarization due to the presence of the dipolar MA molecule[55]. The Rashba effective model was developed in the context of a two-dimensional situation, but in a three-dimensional material, the spin texture on different slices of the Brillouin zone varies. Both the Dresselhaus-type and Rashba-type spin texture can be present in one material, though they occur on different **k**-point planes. The

Rashba-type spin texture occurs on a plane of **k** points that is perpendicular to the internal polarization direction, which is determined by the orientation of the MA molecule (see **Figure 4h,i**).

We also investigated the dependence of the spin texture on the orientation of the MA molecule (see **Figure 4j-m**). The spin texture depends on the MA orientation, but can always be understood by inspecting the gradient of electrostatic potential in the lattice. Most importantly, in all cases the band edges have consistent spin orientations. I.e., even though distinct Rashba spin splitting occurs in halide perovskites, the band edges always split in a coherent way, resulting in a consistent spin orientation between the band edges, which enables spin-allowed radiative recombination.

3.3. Rashba momentum splitting

In Section 3.2, we assessed the impact of the Rashba spin splitting on the radiative recombination in halide perovskites. In this section, we discuss the second important aspect of the Rashba effect, i.e., the Rashba momentum splitting.

In principle, examining the momentum splitting is simple: performing a first-principles calculation of the band structure allows a quantitative determination of the momentum splitting at the band edges, as illustrated in **Figure 5a**. Four important quantities can be directly extracted from the band structure: the momentum splitting at the CBM (Δk_c) and VBM (Δk_v), and the energy splitting at the CBM (ΔE_c) and VBM (ΔE_v). What matters for radiative recombination is the net difference (Δk_{net}) in the momentum splitting between the CBM and VBM. The splittings Δk_c and Δk_v are defined as the ones where ΔE_c and ΔE_v achieve the largest magnitude among all directions in the momentum space. In principle, the momentum shifts are vector quantities, but according to our tests the shifts at the CBM and VBM are close to collinear in all cases.

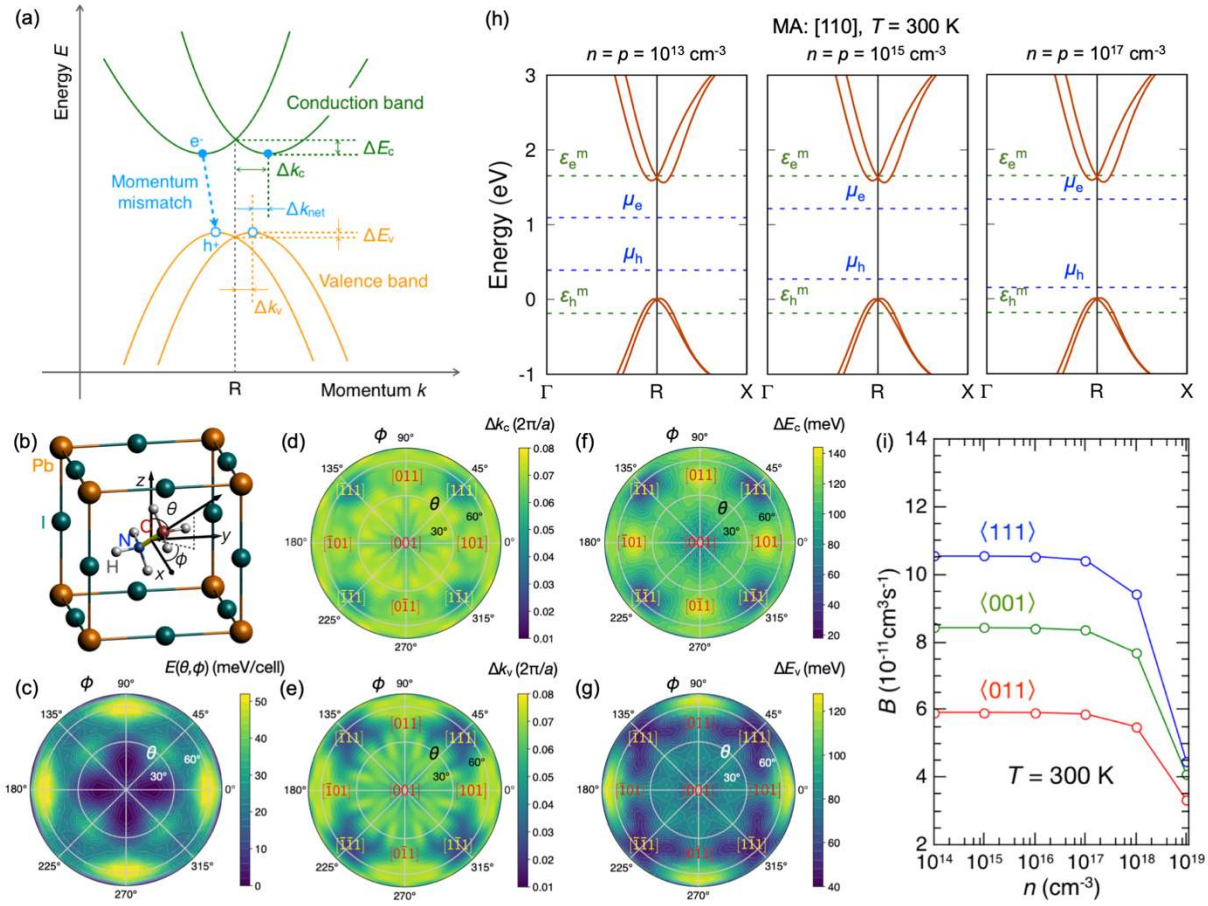

Figure 5. a) Schematic band structure of $MAPbI_3$, illustrating momentum mismatch between the band edges. The light-blue solid circles denote photogenerated electrons (e^-); light-blue open circles denote holes (h^+). b) Crystal structure of $MAPbI_3$. The MA orientation is characterized by the angles θ and φ. c) Energy $E(\theta,\varphi)$ of a $MAPbI_3$ unit cell as a function of θ and φ, referenced to the energy minimum as a function of MA orientation. d,e) Momentum splitting at the CBM (Δk_c) and VBM (Δk_v) as a function of θ and φ. f,g) Energy splitting at the CBM (ΔE_c) and VBM (ΔE_v) as a function of θ and φ. Adapted with permission[56]. Copyright 2018, American Chemical Society. h) Quasi-Fermi levels of electrons (μ_e) and holes (μ_h) and the energy levels of the highest occupied electron (ε_e^m) and hole (ε_h^m) states for three representative carrier densities (10^{13}, 10^{15}, and 10^{17} cm^{-3}). The highest occupied state is defined as the one below which 99% of the carrier density is covered. The MA molecule is oriented along [110], which has the largest Rashba momentum splitting. i) The calculated room-temperature radiative recombination coefficient in $MAPbI_3$ for three representative orientations of the MA molecule. Adapted with permission[56]. Copyright 2018, American Chemical Society.

Nevertheless, even if we consider the momentum splittings as scalar quantities, the problem is non-trivial. As mentioned before, at room temperature the MA molecule can freely rotate, leading to a dynamic crystal structure and a dynamic band structure. Hence, the net momentum splitting is also evolving with time. We addressed this problem by sampling different possible

MA orientations in the cubic phase of $MAPbI_3$ and calculating the energy and momentum splitting for all of the sampled configurations[56]. As shown in **Figure 5b**, two angles (θ and φ) in a spherical coordinate system were used to characterize the orientation of the MA molecule. Then the total energy, momentum splitting and energy splitting were mapped for all MA orientations and shown in **Figure 5c-g**. An important insight from this study is that even though the momentum splitting varies a lot with the MA orientation, the momentum splitting at the CBM and VBM strongly correlates, indicating that the net momentum splitting is actually small.

The net momentum splitting characterizes the momentum mismatch between the CBM and VBM. The impact of this momentum splitting on radiative recombination is further weakened by the fact that at elevated temperatures carriers occupy a finite volume of **k** points. To elucidate how carriers occupy the states near the band edges, we show the quasi-Fermi levels of electrons (μ_e) and holes (μ_h) as well as the energy levels of the highest occupied electron (ε_e^m) and hole (ε_h^m) states for different carrier densities at room temperature in **Figure 5h**. Here we define the highest occupied state as the one below which 99% of the carrier density is covered; in the case of hole states the highest occupied state has the *lowest* energy among those of the occupied states in the valence bands. For the purposes of this analysis, we oriented the MA molecule along [110], which leads to the largest Rashba splitting.

As shown in **Figure 5h**, the quasi-Fermi level of electrons moves closer to the CBM with increasing carrier density. However, the energy (ε_e^m) of the highest occupied electron state remains almost constant as the carrier density is increased. This behavior can be understood based on Equation (9). A higher carrier density is not achieved by occupying more states but by changing the quasi-Fermi level. With a higher quasi-Fermi level, the Fermi occupation factor of each state is increased, which leads to a higher carrier density with the same set of occupied states. Only when the quasi-Fermi level moves above the band edge do states at higher energies become occupied (an effect commonly referred to as phase-space filling[90]); this happens only

at very high carrier densities (> 10^{18} cm^{-3}), in the so-called degenerate limit. Even at the very low carrier density of 10^{13} cm^{-3}, ε_e^m is already higher than the energy of the conduction band at the R point, which means that the electrons occupy a range of momenta that is larger than the magnitude of the Rashba momentum splitting. The same discussion also applies to holes. As a consequence, the occupied electron and hole states have a large overlap in momentum. At finite temperatures, the Rashba momentum splitting therefore does not lead to momentum-mismatched forbidden transitions. It will only have a secondary effect on radiative recombination, through the small misalignment of the highly-populated electron and hole states in the vicinity of the CBM and VBM.

3.4. Quantitative evaluation of the radiative recombination coefficient

Quantitatively, we also calculated the radiative recombination coefficient at room temperature at a function of carrier density for three representative high-symmetry MA orientations[56]. Since the extrema of the momentum and energy splitting always occur at the high-symmetry orientations (see **Figure 5d-g**), an inspection of the high-symmetry configurations captures the upper and lower bounds of the radiative recombination coefficient. As shown in **Figure 5i**, the *B* coefficient is more or less constant at low carrier densities and only starts declining noticeably at densities above 10^{17} cm^{-3} due to the so-called phase-space filling effect[90], which is the effect described in our discussion of the quasi-Fermi levels and carrier occupation (**Figure 5h**) in Section 3.3. Since in solar cells the photogenerated carrier density is relatively low (10^{15} – 10^{16} cm^{-3}), the *B* coefficient is almost independent of carrier density. When the orientation of the MA molecule changes from ⟨111⟩ to ⟨110⟩, the *B* coefficient decreases by less than a factor of two. Our calculated value of the *B* coefficient is around 10^{-10} cm^3s^{-1}. This finding challenges the result by Azarhoosh et al.[71], who argued that due to the Rashba momentum splitting the *B* coefficient of $MAPbI_3$ is less than 10^{-12} cm^3s^{-1}. The rigorous treatment outlined above shows that the *B* coefficient of $MAPbI_3$ is actually comparable to values in conventional direct-gap

semiconductors such as GaAs[91].

3.5. The effects of dynamic disorder

In Sections 3.2 – 3.4 we discussed the impact of the Rashba splitting on radiative recombination, for which the calculations were performed on cubic unit cells with the MA molecule consistently aligned along the same direction in all periodically repeated cells. In reality, the MA molecules are dynamically disordered. In this section, we discuss the progress that has been made in accounting for the dynamic disorder effect.

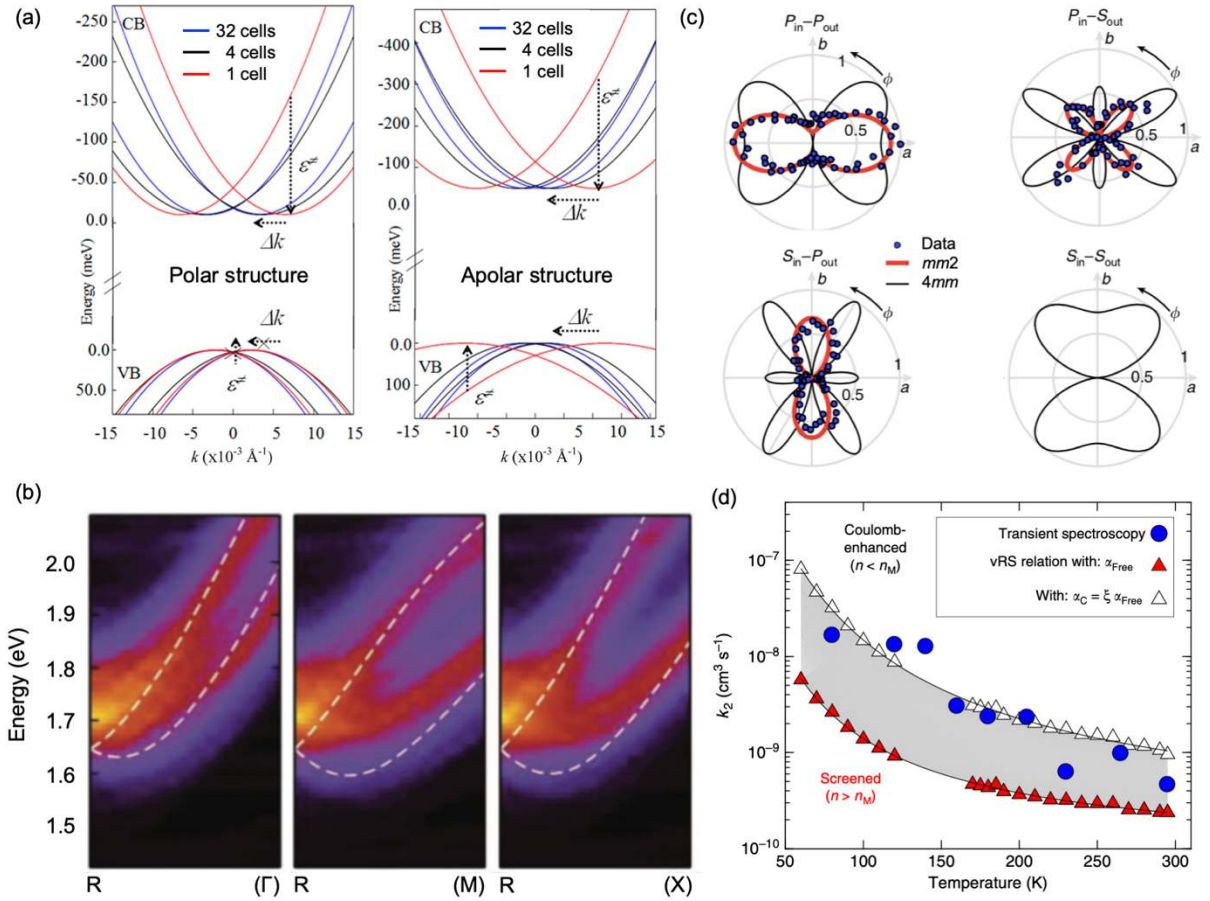

Figure 6. a) Band structure of $MAPbI_3$ for globally polar and apolar structures as defined in the text. The lines of different colors correspond to different supercell sizes. Adapted with permission[34]. Copyright 2016, American Chemical Society. b) Conduction-band structure of $MAPbI_3$ at $T = 0$ K (white dashed line) and $T = 350$ K (heat map). Adapted with permission[58]. Copyright 2018, Wiley. c) Polar plots of the SHG-RA data (blue dots) from the (100) surface of $MAPbI_3$ for different incident and outgoing polarizations. The radial direction represents the normalized magnitude of the SHG intensity and the azimuthal angle φ the orientation of the light scattering plane relative to the tetragonal a-axis. Adapted with permission[88]. Image used

 d) Radiative recombination coefficient of the orthorhombic phase of $MAPbI_3$ as a function of temperature. The blue circles show the experimental data from transient spectroscopy. The solid and open triangles show the calculated radiative recombination coefficient without and with the enhancement by exciton formation. Adapted with permission[59].

To inspect the effect of dynamic disorder, Etienne et al.[34] investigated the Rashba splitting in $2 \times 2 \times 2$ supercells of the tetragonal phase of $MAPbI_3$ (see **Figure 1c**), which in total contain 32 formula units. They oriented the MA molecules in a parallel or anti-parallel manner to form the so-called globally polar and apolar structures[92]. Starting from these two supercells, they performed *ab initio* molecular dynamics simulations at room temperature for ~12 ps. After a proper thermal equilibration, they calculated the band structures of both the polar and apolar configurations shown by the blue lines in **Figure 6a**. Due to the imposition of the tetragonal cell shape, the MA molecules cannot freely rotate at room temperature, and the equilibrated polar and apolar configurations have similar MA orientations as their initial configurations. To obtain a comparative understanding, Etienne et al. examined another four structures by cutting out four-formula-unit and one-formula-unit cells from both the equilibrated polar and apolar configurations. They calculated the band structures of these structures as shown by the black and red lines in **Figure 6a**. With this approach they found that, for both the polar and apolar configurations, the Rashba splitting decreases with increasing cell size, which means that in realistic structures the Rashba effect gets further quenched compared to the fully polarized cubic unit cells discussed in Section 3.3. Since even in the polarized cubic unit cells the impact of the Rashba splitting on radiative recombination is minor, one expects a negligible influence.

Another approach to this problem is offered by examining the finite-temperature band structure of cubic $MAPbI_3$[58] calculated by accounting for the temperature-induced fluctuations[93] (**Figure 6b**). The white dashed lines show the static band structure calculated at $T = 0$ K, where

one observes relatively large splitting along the R → M and R → X directions. However, once temperature-induced fluctuations are taken into account, as shown by the "heat map" at $T = 350$ K in **Figure 5**, the Rashba splitting basically gets washed out. The conclusion is that finite-temperature lattice fluctuations weaken the effect of the Rashba splitting and thus its impact on radiative recombination.

Frohna et al.[88] approached the problem experimentally. They investigated the "averaged" point group symmetry of $MAPbI_3$ using the second harmonic generation rotational anisotropy (SHG-RA) technique, which is much more sensitive than diffraction-based techniques in distinguishing between centrosymmetric and non-centrosymmetric structures. As shown in **Figure 6c**, for all polarization channels ($P_{in} - P_{out}$, $P_{in} - S_{out}$, and $S_{in} - P_{out}$) the experimental data fit well with the angular dependence of the SHG intensity for the *mm2* point group of a crystal with space group *I4/mcm*, which is centrosymmetric. Hence, the averaged structure of $MAPbI_3$ maintains inversion symmetry. Nevertheless, the spatial resolution of this technique is ~10 μm, which cannot rule out the existence of a local Rashba effect within domains of smaller than 10 μm in size.

Next, we briefly discuss exciton formation. It does not affect the Rashba splitting, but potentially influences the radiative recombination coefficient. Davies et al.[59] inspected the impact of excitons on the radiative recombination in $MAPbI_3$. Based on the Elliott theory, they derived a so-called Coulomb enhancement factor (ξ) on the radiative recombination coefficient due to exciton formation, using the exciton binding energy obtained by fitting the experimental absorption spectrum as input. As shown in **Figure 6d**, the exciton formation enhances the radiative recombination coefficient by a factor of four at room temperature. From both theory and experiment, the obtained radiative recombination coefficients are between 10^{-10} and 10^{-9} cm^3s^{-1}, similar to our first-principles results[56] with a slight enhancement due to the presence of excitons. Again, the conclusion is that radiative recombination in $MAPbI_3$ is strong.

Finally, we discuss the potential influence of polarons on radiative recombination. Due to the Coulomb interaction between charge carriers and ions, polarons could form by trapping charge carriers with collective displacements of ions in the lattice. The likelihood of the formation of a polaron is determined by the difference between the reciprocals of the static (ε_0) and high-frequency (ε_∞) dielectric constants. In the case of halide perovskites, ε_0 is significantly larger (>30) than ε_∞ (~5-10)[94], indicating that large polarons will likely form. As shown by Emin[95], there exists a short-range repulsion between oppositely charged large polarons due to the interference between the associated displacement fields. This short-range repulsion may even overwhelm the attractive Coulomb interaction between the oppositely charged large polarons, which would impede the recombination between charge carriers. Recently, a number of experimental studies[32,36–38] have been performed to study the impact of large polarons on the radiative recombination in halide perovskites, which qualitatively revealed a slowdown of the radiative recombination due to the formation of large polarons. Explicit calculations of the impact of polaron formation on the radiative recombination coefficient are still lacking.

Therefore, despite the arguable existence of Rashba splitting in halide perovskites, it has a minor impact on radiative recombination. Having achieved this important insight, we can now look back at previous reports based on $k \cdot p$ theory[96] or first-principles calculations[97] that neglected the SOC effect. At the time, the neglect of SOC was an untested assumption, but the results described above support its validity. Indeed, those more approximate calculations[96,97] produced B coefficients around 10^{-10} – 10^{-9} cm^3s^{-1}, close to the recent more accurate results. Overall, we conclude that, while SOC may have other important consequences (as discussed in Section 4), the resulting Rashba effect has a very limited impact on the radiative recombination coefficient in halide perovskites; the coefficient is similar in magnitude to conventional direct-gap semiconductors.

4. Auger recombination

As documented in Section 3, radiative recombination is strong in halide perovskites, and light-emitting applications are therefore possible. However, the operation of LEDs requires much higher carrier densities than in solar cells, and at these higher densities the third-order Auger recombination becomes critical. As demonstrated in conventional nitride LEDs, Auger recombination causes the observed efficiency droop at high carrier densities[98]. Experimental measurements[39–41,43] showed that the third-order recombination coefficient of halide perovskites is significantly higher than that of many conventional semiconductors with similar band gaps. However, experiments alone do not determine whether Auger recombination is responsible, since other processes such as carrier leakage[47] or drift-induced leakage[99] can also lead to third-order coefficients in carrier dynamics. Moreover, the fundamental electronic-structure origin of the strong third-order coefficient cannot be intuitively extracted from experiments. A direct first-principles computation of Auger recombination is particularly valuable for tackling this problem.[57] In this section, we outline the key insights into the Auger recombination mechanisms in halide perovskites from first-principles calculations and discuss the potential avenues to reducing the Auger recombination.

4.1. Unexpectedly strong Auger and its origin

Figure 7a,b shows our calculated first-principles band structure of the cubic phase of $MAPbI_3$[57] and indicates the four states involved in an eeh or hhe Auger process. Using the methodology described in Section 2.2, we calculated the Auger recombination coefficients for the eeh and hhe processes as a function of scissor-shifted band gap as shown in **Figure 7c**. A scissor-shift operation is commonly used in these studies to probe the effect of key features in the band structure (to be discussed in detail later) or to examine alloying effects. At the experimental band gap of $MAPbI_3$ (1.6 eV, indicated by the black dashed lines), the obtained Auger coefficients are 2.7×10^{-29} cm^6s^{-1} for eeh and 4.6×10^{-29} cm^6s^{-1} for the hhe process. The calculated total Auger coefficient (7.3×10^{-29} cm^6s^{-1}) agrees well with the experimentally

measured ones, which range from 5.4×10^{-29} to 1.6×10^{-28} cm^6s^{-1}[39–41,43].

To put these numbers into context, we compare the Auger coefficient of $MAPbI_3$ with those of other semiconductors. **Figure 7d** depicts the Auger coefficients of a number of semiconductors compiled by Bulashevich and Karpov[100]. We can see that the Auger coefficients of the conventional semiconductors with band gaps larger than 1 eV are all around 10^{-30} cm^6s^{-1}. Unexpectedly, the Auger coefficient of $MAPbI_3$ is two orders of magnitude larger than that of other semiconductors with similar band gaps.

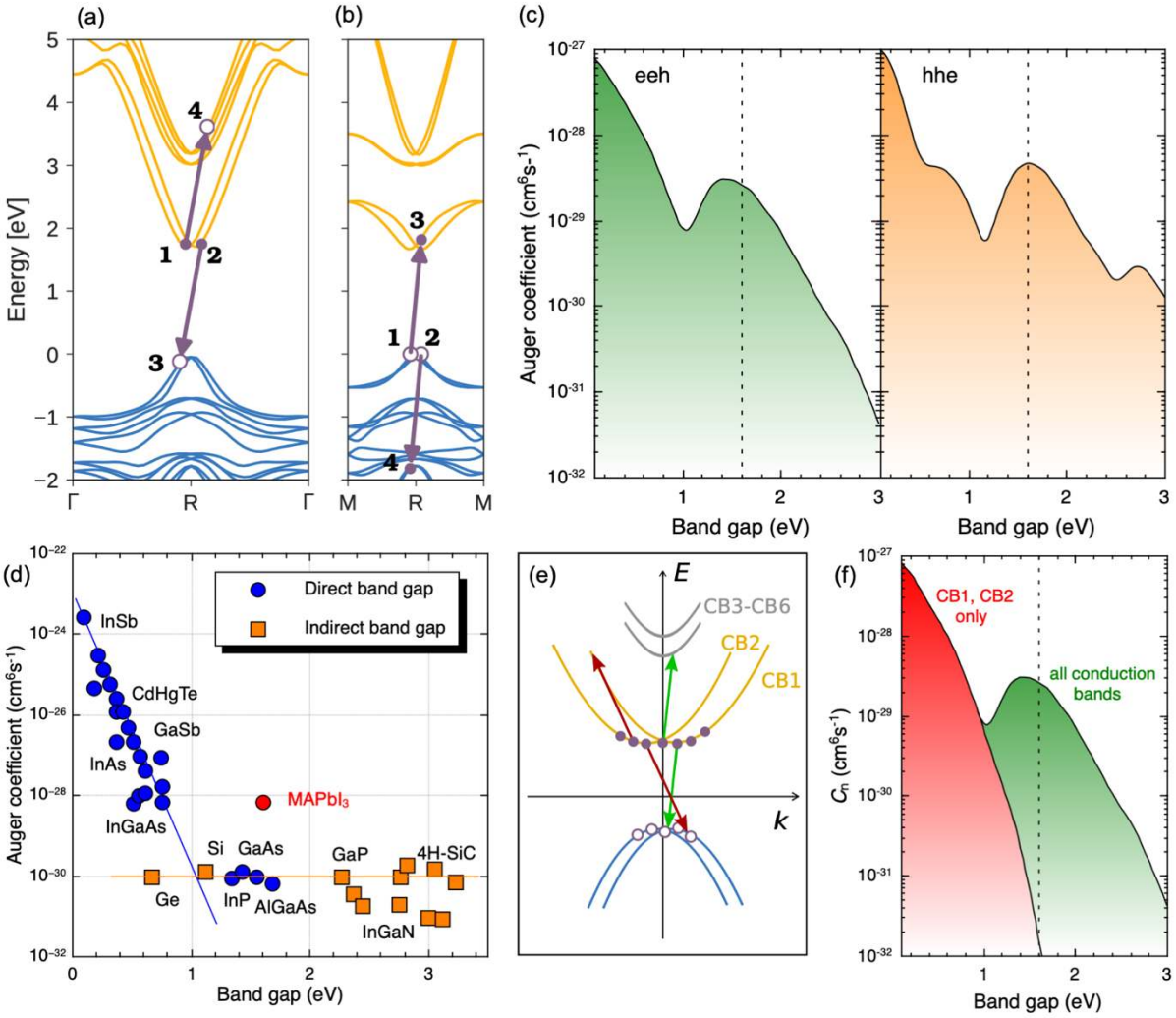

Figure 7. a,b) First-principles band structure of $MAPbI_3$ along different high-symmetry paths in the Brillouin zone, in which example eeh and hhe processes are indicated. Adapted with permission[57]. Copyright 2018, Wiley. c) Calculated Auger coefficient as a function of scissor-shifted band gap for both eeh and hhe processes. The black dashed line shows the experimental band gap of $MAPbI_3$ (1.6 eV). Reproduced with permission[57]. Copyright 2018, Wiley. d)

Comparison of the Auger coefficient of $MAPbI_3$ to other semiconductors. Reproduced with permission[100]. Copyright 2008, Wiley. e) Schematic illustration of intraband (red arrows) and interband (green arrows) Auger processes. The purple solid spheres represent electrons and the purple open circles holes. Adapted with permission[57]. Copyright 2018, Wiley. f) The corresponding eeh Auger coefficient for the intraband and interband transitions. Reproduced with permission[57]. Copyright 2018, Wiley.

A better understanding of the physical mechanisms behind the unexpectedly strong Auger coefficient of $MAPbI_3$ can be achieved by examining **Figure 7c**. In both eeh and hhe processes there is a broad peak in the Auger coefficients, which reaches its maximum at almost exactly the band gap of $MAPbI_3$. To address the origin of this broad peak, we distinguish between two types of Auger processes: intraband vs. interband[57]. **Figure 7e** schematically shows the intraband and interband processes for eeh Auger. CB1 and CB2 correspond to the same band in the absence of SOC; even though they are slightly split due to the Rashba effect as discussed in Section 3.1, we consider CB1 and CB2 effectively as one band when distinguishing between intraband and interband processes. If the Auger process involves CB1 and CB2 only, it is labeled an intraband process (red arrows); when higher-lying conduction bands are involved, we label it an interband process (green arrows). The calculated Auger coefficients as a function of band gap for these two scenarios are presented in **Figure 7f**. The broad peak completely vanishes if only CB1 and CB2 are included. In this case, the Auger coefficient is more than three orders of magnitude lower than the case where all conduction bands are included. It becomes immediately apparent that the unexpectedly high eeh Auger coefficient of $MAPbI_3$ is due to a resonance of the band gap with interband transitions to a complex of higher-lying conduction bands. In fact, the energy difference between CB3-CB6 and CB1-CB2 is caused by strong SOC splitting in the halide perovskites. A similar resonance exists for the hhe process: as shown in **Figure 7b**, a complex of valence bands occurs at an energy of approximately one band gap below the VBM. Unlike the splitting in the conduction bands, this resonant energy difference in the valence bands is not caused by SOC.

As a second effect, the carrier distribution at the band edges also enhances the Auger coefficient. Due to the Rashba splitting, carriers (especially electrons) occupy states over a wide range of momenta (see the schematic in **Figure 7e**). The spread of the carrier distribution leads to an increase in the number of eeh and hhe processes that satisfy momentum conservation, resulting in an additional enhancement of the Auger coefficient. In Ref.[57], we compared the Auger coefficient of $MAPbI_3$ for two structures: one including the full relaxation of the lattice, which leads to a large distortion of the Pb-I octahedron that produces a significant Rashba splitting; the other constrained to have no distortion of the Pb-I octahedron and thus no Rashba splitting. We found that the removal of the lattice distortion reduces the Auger coefficient by one order of magnitude.

In summary, the Auger recombination in halide perovskites is unexpectedly strong—two orders of magnitude larger than in conventional semiconductors with similar band gaps. This determination establishes that Auger recombination is indeed responsible for the experimentally observed high third-order coefficient. The exceptionally high Auger coefficient primarily stems from a coincidental resonance of the band gap with states that are roughly one band gap away from the band edges. This large value of the Auger coefficient would definitely limit the efficiency of light-emitting devices, and it could also impact solar cells.[101] It is therefore important to examine approaches to reduce the Auger coefficient in halide perovskites, as discussed in detail in Section 4.2.

4.2. Band-structure engineering

The Auger process requires simultaneous energy and momentum conservation, and thus we can suppress Auger recombination in a material by making it harder to satisfy these conservation rules. This can be achieved in one of two ways: eliminating the near-resonance between the band gap and the resonant band splitting, and reducing the lattice distortions so that the initial charge carriers are more concentrated in the Brillouin zone[57]. Here we discuss both of these

methods in detail with newly computed results and show how they can be achieved via band-structure engineering.

Band-structure engineering can be achieved via chemical substitution or strain. Strain engineering for desired electronic-structure properties is hypothetically possible for halide perovskites because in actual photovoltaic cells the halide perovskite is sandwiched between charge collection layers, and a mismatch between lattice parameters can occur at the interface. In traditional semiconductors, this lattice mismatch can be used to strain a crystal and deform the electronic structure[102]. While strain engineering is in principle possible, recent computational[103] and experimental[104,105] studies have shown that predictably modifying the electronic structure of $MAPbI_3$ is difficult, due to a combination of the occurrence of competing phases[104] and the formation of domains with different molecular orientations caused by the change in lattice parameters[103,106,107]. As such, we focus on chemical substitution as the means to control the electronic structure.

4.2.1 Engineering of the band gap

As discussed in Section 4.1, the strong Auger recombination in $MAPbI_3$ is mainly caused by the presence of conduction and valence bands that are roughly one band gap away from the band edges. To understand how chemical substitution impacts these bands, we explore the space of frequently investigated halide perovskites (ABX_3) by testing combinations of commonly considered ions as tabulated in **Figure 1a**. For simplicity and consistency, we consider single-formula-unit cubic unit cells of each material. The band structure of each material is computed using the HSE hybrid functional[87] (with a fixed mixing parameter of 0.55) and plotted along the high-symmetry path $\widetilde{\mathrm{X}} - \mathrm{R} - \mathrm{M}$ in **Figure 8a**. Since for hybrid perovskites the presence of the organic molecules breaks the inversion symmetry, X, Y, and Z are in principle inequivalent. In this case, $\widetilde{\mathrm{X}}$ is chosen from (X, Y, Z) so that $\widetilde{\mathrm{X}} - \mathrm{R}$ has the largest momentum splitting at the CBM (Δk_c). For inorganic perovskites, there is no Rashba splitting and $\widetilde{\mathrm{X}}$ is equal to X.

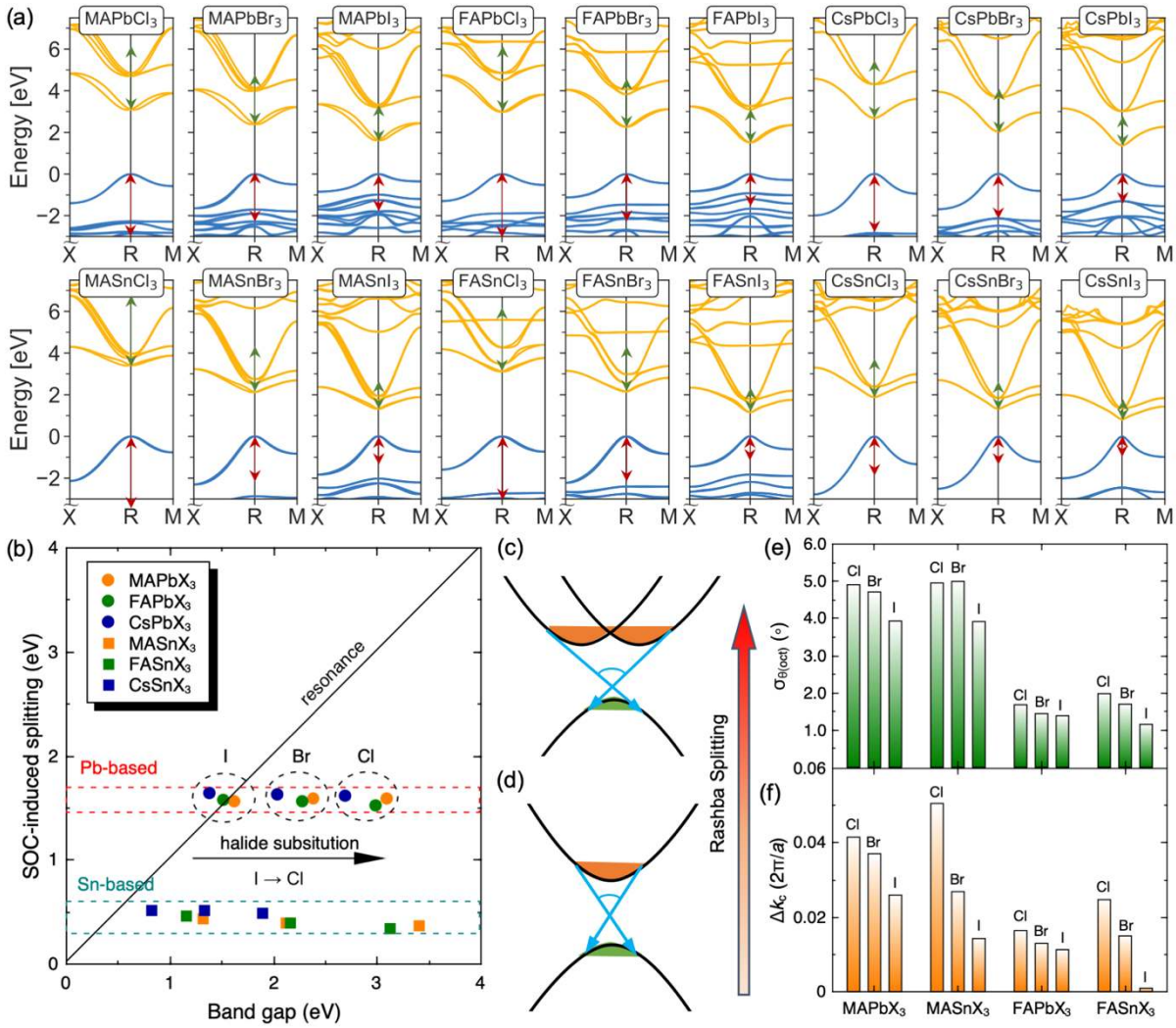

Figure 8. a) First-principles band structures of ABX_3 using the HSE hybrid functional, where A = (MA, FA, Cs), B = (Pb, Sn), X = (Cl, Br, I). Each band structure is plotted along the high symmetry path $\widetilde{X} - R - M$. The red (green) arrows indicate an energy difference equal to the band gap of the compound measured from the VBM (CBM) down (up). b) Relationship between the SOC-induced splitting in the conduction band and the band gap of a set of halide perovskites. The red and cyan dashed lines classify the studied compounds into Pb-based and Sn-based halide perovskites. The black dashed circles divide the Pb-based perovskites into subgroups with different halides. c,d) Schematic illustration of the effect of decreasing structural distortions on the Rashba splitting, affecting the range of momentum states occupied by carriers. e) Chemical trends in the standard deviation of the Pb-I bond angles at the octahedral center in different halide perovskites. f) Chemical trends of the corresponding Rashba splitting.

We first inspect the impact of chemical substitution on the resonance in the conduction bands, relevant for the eeh Auger process. We extract from the band structures the SOC-induced splitting in the conduction bands and the band gap of different halide perovskites and plot them in **Figure 8b**. It can be seen that the SOC-induced splitting is mainly determined by the B-site

cation. The Pb-based perovskites have similar SOC-induced splittings (average: 1.56 eV, standard deviation: 64 meV), more than three times larger than those of the Sn-based perovskites (average: 0.44 eV, standard deviation: 58 meV). This is because the states at the CBM are dominated by the *p* electrons of either Pb or Sn, and Pb is heavier than Sn. In the case of Pb-based perovskites, chemical substitution on the A site has a minor impact on band gap compared to X-site substitution. For Sn-based perovskites, however, A-site substitution significantly influences the band gap. Substituting an inorganic element (Cs) versus an organic molecule (MA or FA) affects the band gap more strongly than substitutions on the X site. As a result, $CsSnCl_3$ has a smaller band gap than $MASnBr_3$ and $FASnBr_3$. For all of the $APbI_3$ compounds the resonance with the SOC-induced splitting, which leads to strong eeh Auger recombination, is a big concern. Fortunately, chemical substitution on the X site can significantly increase the band gap, which allows a suppression of the resonance. This is consistent with the experimental fact that alloying $MAPbI_3$ with Cl reduces the Auger coefficient by around one order of magnitude[45,108].

We note that since higher-lying conduction bands are present, additional resonances may occur. When changing the X site from I to Cl, the band gap increases, which helps to get rid of the resonance with the SOC-induced splitting shown in **Figure 8b**. Unfortunately, this increase in the band gap may bring the band gap into resonance with the energy difference to a higher-lying conduction band (see the green arrows in **Figure 8a**), which is particularly serious for $FAPbCl_3$. Hence, the impact of Auger recombination is potentially as high in $FAPbCl_3$ as it is in $FAPbI_3$. As a consequence, when alloying $FAPbI_3$ with Cl, the Cl concentration should not be too high.

As discussed above, a similar resonance occurs for the hhe Auger process, though the splitting of bands in the valence band is not caused by SOC. In **Figure 8a** the red arrows indicate an energy difference equal to one band gap of the specific perovskite measured from the VBM

down. We clearly see that in all of the $APbX_3$ compounds there is a complex of valence bands that occurs at approximately one band gap below the VBM. These bands are comprised mainly of halogen states. Chemical substitution on the halogen site changes the band gap and the resonant energy difference in the valence bands in concert, and thus cannot be used to suppress the hhe Auger process. The Sn-based perovskites, on the other hand, have much smaller band gaps and much larger band splittings in the valence bands, and therefore changing the B site from Pb to Sn can significantly reduce the hhe Auger coefficient. The only exceptions are $FASnCl_3$ and $FASnBr_3$, for which the hhe resonance still exists. In this case, additional A-site and X-site substitution can be used to get rid of the hhe resonance.

In summary, both the eeh and hhe Auger coefficients of ABX_3 perovskites can be significantly reduced through band-structure engineering. X-site substitution is beneficial for reducing the eeh Auger coefficient, and B-site substitution can help to lower the hhe Auger coefficient.

4.2.2 Engineering of structural distortions

A more subtle method to suppress the Auger recombination in halide perovskites is to decrease the Rashba splitting at the band edge by engineering the distortions of the inorganic lattice. As shown by the schematics in **Figure 8c,d**, when the Rashba splitting at the CBM is reduced electrons are concentrated in a smaller region of momentum space. We characterize the maximum range of momentum that an Auger process can make use of by the angle between the two extreme directions (the light-blue arrows in **Figure 8c,d**) formed by connecting one electron and one hole. The range of momentum is reduced when the Rashba splitting is decreased. Consequently, it is much more difficult to conserve momentum when the Rashba splitting is small. We recently demonstrated how this concept can be applied to reduce the Auger coefficient.[57] Our simulations showed that both the eeh and hhe Auger coefficients can be reduced by one order of magnitude if the lattice distortions and thus the Rashba splitting are removed. In Section 3.5 we discussed how finite-temperature and dynamic disorder effects

smear out the effects of Rashba splitting compared to the static band structure; however, the distribution of carriers over a larger range of momenta persists. Here we perform a comprehensive investigation of how the momentum-space splitting correlates with the lattice distortion.

The lattice distortion in a perovskite structure can be quantified by the so-called bond-angle variance, which is the variance of all the angles subtended by the bonds to the central atom of the octahedron[109]:

$$\sigma^2_{\theta(\mathrm{oct})} = \frac{1}{11}\sum_{i=1}^{12}(\theta_i - 90°)^2. \quad (14)$$

Using the hybrid-functional band structures of the 18 halide perovskites shown in **Figure 8a**, we inspect the chemical trends in the degree of Rashba splitting (as measured by the maximal Δk_c) and the bond-angle standard deviation given by $\sigma_{\theta(\mathrm{oct})}$ in **Figure 8e,f**. Since the Cs-based perovskite compounds exhibit inversion symmetry and therefore have no Rashba splitting, they are not included in **Figure 8e,f**.

It is clear that in all subgroups of halide perovskites shown there is a correlation between the lattice distortion and the Rashba splitting: a larger distortion increases the Rashba splitting by breaking the inversion symmetry to a larger extent. **Figure 8e,f** shows that the lattice distortion is sensitive to X-site substitution. Substituting I by Br or Cl increases the lattice distortion and thus the Rashba splitting, which enhances Auger recombination. Therefore, to engineer the Auger coefficient by chemical substitution on the X site, there is a trade-off between avoiding the band-gap resonance and reducing the Rashba splitting; this may be the reason why the Auger coefficient of $MAPbBr_3$ is actually slightly larger (by a factor of three) than that of $MAPbI_3$[41]. We note that the sensitivity to X-site substitution is even more pronounced for the Sn-based perovskites.

Replacing MA with FA or Cs significantly reduces the Rashba splitting, since FA and Cs are less polar than MA, leading to smaller (or zero, in the case of Cs) lattice distortions. Combined with the insights gained in Section 4.2.1, we conclude that the Auger coefficient can be minimized when the A site is Cs, the B site is Sn, and the X site is Br.

Nevertheless, this is purely based on a consideration of relation between band structure and Auger recombination. For systematic materials and device design we still need to take into account the desired wavelength of the emitted light, the defect physics, and the phase stability of the materials; for the latter the hybrid perovskites have advantages over inorganic perovskites. There are potentially more trade-offs to be considered during a careful optimization of the chemical composition to achieve the best light-emitting performance. We have tabulated the key quantities of all the perovskite compounds studied that are relevant for band-structure engineering in the Supporting Information. This information will allow for optimizing the chemical composition of halide perovskites toward enhanced light-emitting performance.

4.3. Hot-carrier relaxation

Auger recombination causes charge carriers to be promoted to higher-lying states; these hot carriers will relax back to the band edges. As schematically shown in **Figure 9a**, there are two possible pathways for the relaxation of hot electrons: radiative and nonradiative. In the radiative pathway, electrons relax back to the band edges by emitting photons. In this case, even though Auger recombination takes place, the energy of the recombination process is not lost and ultimately still results in emission of a photon (which, due to the resonance that causes Auger to be strong, would have roughly the same energy as band-gap photons). Such a radiative process would thus be beneficial for the operation of LEDs. In contrast, when the relaxation occurs through the nonradiative pathway, the energy of the hot carriers is released to phonons, i.e., dissipated as heat. In this section, we focus on the relaxation of hot electrons. The behavior of hot holes is expected to be similar.

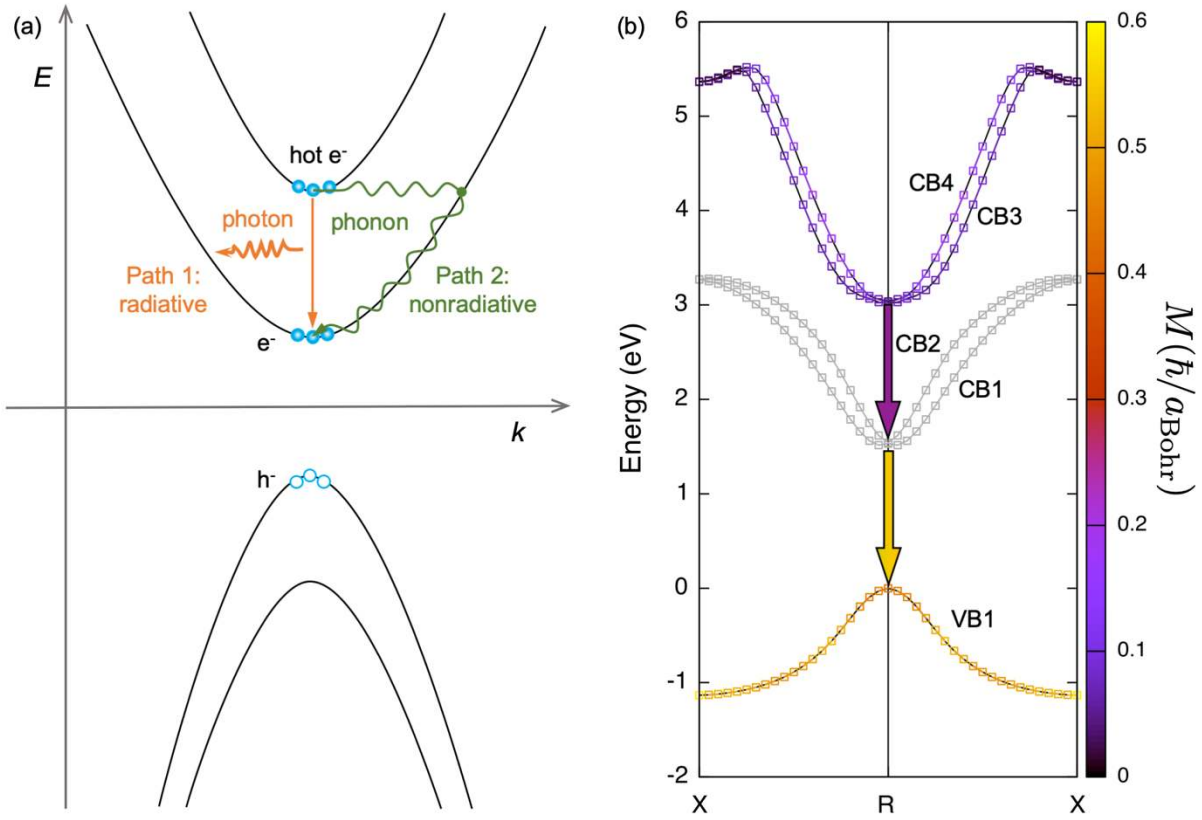

Figure 9. a) Schematic illustration of two pathways (radiative vs. nonradiative) for hot electrons to relax back to the CBM. The light-blue solid spheres represent electrons (e^-) and light-blue open spheres holes (h^+). b) First-principles band structure of $MAPbI_3$, in which the color of the valence band indicates the magnitude of the momentum matrix elements (M) for the transitions between the lowest conduction band (CB1) and the highest valence band (VB1). The color of the higher-lying conduction bands (CB3 and CB4) depicts the magnitude of the momentum matrix elements for the transition between these bands and CB1. CB1 and CB2 result from a Rashba splitting; we denote CB1 as the outer branch and CB2 as the inner branch. The same is true for CB3 and CB4. In this notation, CB1 is the lowest conduction band. For the valence bands, Rashba splitting is small and the two bands are almost degenerate. We only show VB1, corresponding to the highest valence band (the outer branch).

To determine the nature of the relaxation of hot carriers in halide perovskites, we calculate the momentum matrix elements (which determine the dipole transition strength) for transitions between the two higher-lying conduction bands (CB3 and CB4) and the lowest conduction band (CB1); the magnitude of these matrix elements is shown by the color of CB3 and CB4 in **Figure 9b**. We note that even though CB3 and CB4 have opposite spin orientations, the transition between CB4 and CB1 is not strictly forbidden and its total momentum matrix elements are only slightly weaker than those of the transition between CB3 and CB1. For comparison, we

also show the magnitude of the momentum matrix elements for the radiative transition between CB1 and VB1, indicated by the color of the highest valence band (VB1). It can be seen that the radiative transitions from the higher-lying to the lower-lying conduction bands are somewhat weaker than the transitions between CB1 and VB1, but only by a factor of three. This means that the radiative relaxation pathway is of similar strength to the radiative transition across the band gap.

This comparison of transition strengths might give the impression that radiative transitions from CB3/CB4 to CB1/CB2 are likely to happen. However, what really matters is whether radiative recombination will dominate over nonradiative recombination. We therefore compute the radiative transition rate (r) between CB3/CB4 and CB1 based on first-order perturbation theory for a two-state system, which is given by[63]

$$r = \frac{n_r e^2}{\pi \epsilon_0 m_e^2 c^3 \hbar^2} (\varepsilon_1 - \varepsilon_2) |M_{12}|^2, \quad (15)$$

where n_r is the refractive index, e the elementary charge, ϵ_0 the vacuum permittivity, m_e the free electron mass, c the speed of light and $\hbar$ the Planck constant. ε_1 and ε_2 are the energy levels of the two states and M_{12} the momentum matrix elements of the radiative transition between states 1 and 2. Using this formula, we obtain the radiative transition rate as 2.8×10^7 s^{-1}, which corresponds to a lifetime of 35.7 ns.

With regard to the nonradiative channel, carriers first need to transition from CB3/CB4 to CB1/CB2. We assume this will happen with a rate comparable to intervalley scattering, which has been extensively studied in traditional semiconductors and been found to occur on a time scale of a few ps[110]. Subsequent relaxation within CB1/CB2 to the CBM quickly happens assisted by phonon emission on a sub-picosecond time scale[111]. While these lifetimes are only estimates, the four-order-of-magnitude difference in rates between the radiative and nonradiative pathways indicates that hot carriers in halide perovskites will overwhelmingly

relax nonradiatively, thus leading to energy dissipation and efficiency loss. Any hope of recovering some of the energy spent on Auger recombination through radiative emission is in vain.

5. The rate-limiting step of carrier recombination

In Section 3, we discussed the role of the Rashba splitting in radiative recombination, showing that the impact is minor and the radiative recombination in halide perovskites is as strong as in conventional direct-gap semiconductors. In this section, we discuss the rate-limiting step of carrier recombination in halide perovskites across a wide range of carrier densities. The discussion will show that it is a misconception to think that carrier lifetime in solar cells can be enhanced by suppressing radiative recombination.

The rigorous determination of the carrier lifetime is a complicated problem, which may involve processes other than carrier recombination. For the purposes of this discussion, we focus on the lifetimes associated with different recombination processes. The total recombination lifetime is limited by the shortest lifetime among all recombination, i.e.,

$$\frac{1}{\tau_{\mathrm{tot}}} = \frac{1}{\tau_{\mathrm{SRH}}} + \frac{1}{\tau_{\mathrm{radiative}}} + \frac{1}{\tau_{\mathrm{Auger}}} = A + Bn + Cn^2 \,, \tag{16}$$

where A, B and C are the defect-assisted SRH, radiative and Auger recombination coefficients, respectively. The B and C coefficients have been calculated using first-principles approaches[56,57] (see Sections 3.4 and 4.1). Defect-assisted recombination was not explicitly discussed in the present report, but reported values for the A coefficient are remarkably consistent. We take a typical value of 5×10^6 s^{-1} obtained by fitting to experiment by Richter et al.[43]

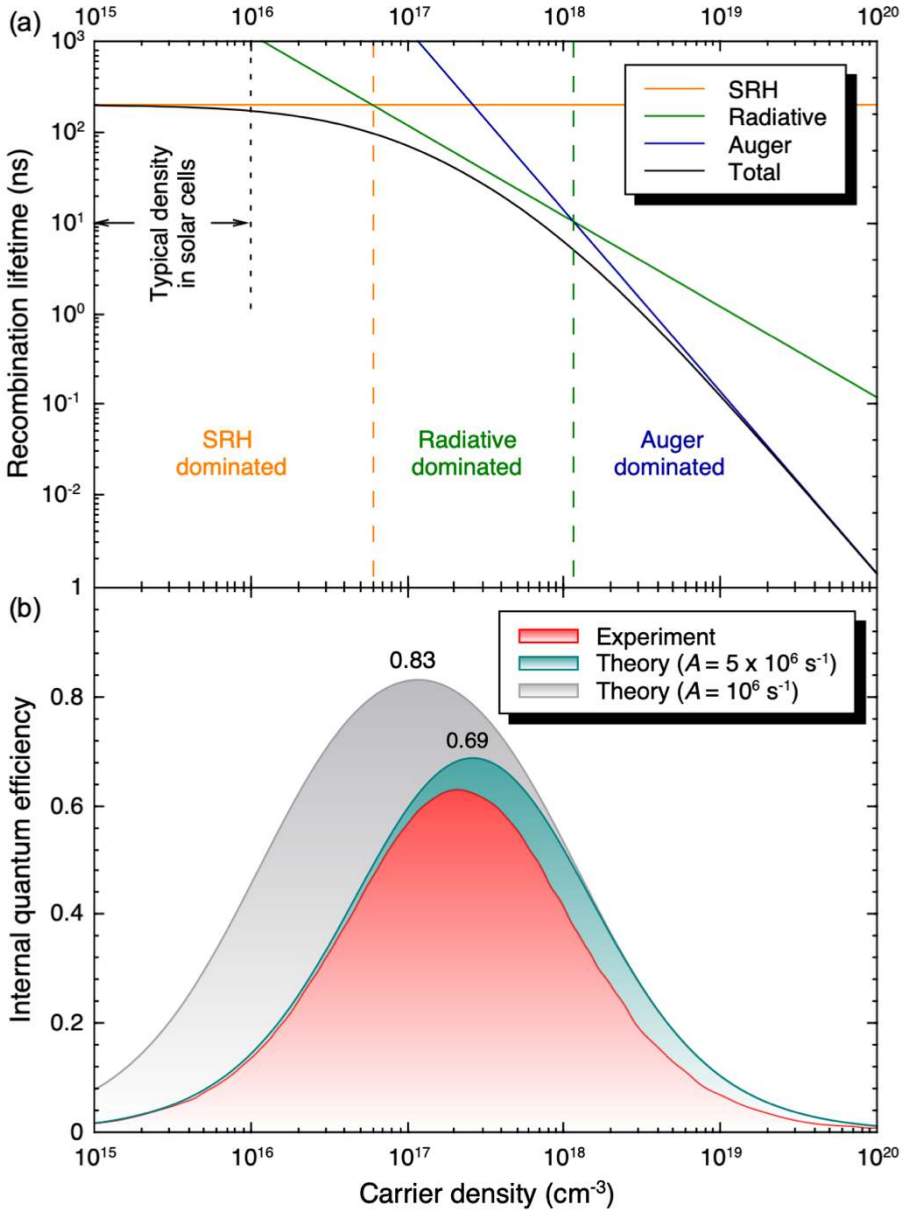

Figure 10. a) Recombination lifetimes as a function of carrier density, revealing the dominant recombination process in different regimes of carrier density. b) Comparison of internal quantum efficiency between theory and experiment[43].

Figure 10a presents the computed total and individual recombination lifetimes as a function of carrier density. Given the form of the rate equation, it is clear that at low carrier densities (< ~6 × 10^{16} cm^{-3}, indicated by the orange dashed line) the total lifetime is limited by the defect-assisted SRH recombination. At very high carrier densities (> ~10^{18} cm^{-3}, indicated by the green dashed line), the lifetime is dominated by Auger recombination. We therefore expect the internal quantum efficiency (the ratio of radiative to total recombination rates) to peak in the intermediate region of carrier densities, where radiative recombination is dominant. For solar

cells, the carrier density is relatively low, usually between 10^{15} and 10^{16} cm^{-3}. In this range, lifetimes are dominated by the SRH process, and radiative recombination has a negligible impact on the total recombination lifetime. Suppressing radiative recombination would not lead to a longer carrier lifetime. However, a low radiative recombination would impede halide perovskites from making efficient LEDs. In fact, halide-perovskite LEDs have been demonstrated already in 2014[23] and the efficiency has been constantly improving[112–122].

Using the recombination coefficients we can also evaluate the internal quantum efficiency η:

$$\eta = \frac{Bn^2}{An+Bn^2+Cn^3}. \quad (17)$$

Figure 10b shows the computed internal quantum efficiency as a function of carrier density compared to experimental data[43]. Both theory and experiment show "droop", i.e., a reduction of the efficiency at high carrier densities. Based on our calculated results (Section 4), we can attribute the droop to strong Auger recombination. Moreover, the theoretical curve (cyan) with a typical A coefficient from the literature[43] ($A = 5 \times 10^6$ s^{-1}) agrees well with the experimental curve[43], indicating that our calculated values for B and C properly capture the physical mechanisms behind the operation of halide-perovskite devices.

As a comparison, we also present another theoretical curve (gray) obtained by assuming a lower A coefficient ($A = 10^6$ s^{-1}). We can clearly see that the peak internal quantum efficiency is enhanced by ~14% when the SRH recombination efficient is reduced by a factor of five, demonstrating the important impact of defect-assisted SRH recombination. Even though a number of studies have been devoted to intrinsic defects and impurities in halide perovskites[54,123–127], the issue of *which* defects are responsible for the experimentally observed SRH recombination is far from settled.

Given the favorable comparison between theory and experiment, we conclude that based on

accurate first-principles calculations the performance of halide perovskites can be reliably described and understood. There is no need to invoke unusual mechanisms such as the Rashba effect to explain the high performance. As indicated by **Figure 10a**, for solar cells the dominant recombination mechanism is the defect-assisted SRH recombination, which should be the central focus in order to understand and control the mechanisms behind the superior performance of halide perovskites in solar-cell applications. For light-emitting applications, the strong Auger recombination causes efficiency droop at high carrier densities. However, as discussed in Section 4.2, there exist potential avenues to reducing the Auger coefficient by band-structure engineering.

6. Summary and outlook

Halide perovskites are highly efficient optoelectronic materials and have shown potential in other emerging applications. A large amount of research effort has been devoted to improving their performance. The *understanding* of the fundamental mechanisms underlying the remarkable performance has lagged behind. In this report, we demonstrated that first-principles calculations can reliably describe carrier recombination processes and elucidate these mechanisms.

We systematically discussed the critical achievements in first-principles simulation of carrier recombination mechanisms in halide perovskites. For radiative recombination we showed that accurate first-principles calculations can clear up a number of misunderstandings and misconceptions in the field. An important message is that the SOC-induced Rashba splitting has only a minor impact on radiative recombination.

Spin-orbit interactions *do* play an important role in other recombination processes, however. In particular, the SOC-induced spitting in the conduction bands significantly impacts the eeh Auger recombination by creating a resonance between the band gap and the SOC-induced

splitting in the conduction bands. A similar resonance occurs in the valence bands, though it is not caused by SOC. These resonances as well as severe lattice distortions significantly enhance the Auger coefficient in halide perovskites, which is two orders of magnitude higher than other conventional semiconductors with similar band gaps. Fortunately, there are potential avenues to suppress the Auger coefficient through band-structure engineering in perovskites.

A critical analysis of the rate-limiting step for carrier recombination in halide perovskites showed that under the operation condition in solar cells the defect-assisted SRH recombination is dominant. This has two important implications. First, it is conceptually misleading to try to enhance the carrier lifetime by suppressing radiative recombination. Second, in order to elucidate the fundamental mechanisms that govern the performance of halide perovskites and to further improve their performance, research efforts should be directed towards defects and defect-assisted SRH recombination. Early studies[123,128] suggested concepts such as "defect tolerance", but the SRH recombination coefficients extracted from experiment are not particularly lower than values in other semiconductors, in which defects have been accepted to play a limiting role. First-principles calculations[127,129] and experiments[12,130,131] have demonstrated that deep-level defects are definitely present. What is still missing is a link between the defects that are known to be present and the observed SRH recombination rates; i.e., a microscopic identification of the key centers that are limiting efficiency. Even though there have already been attempts[53,54] to quantify the defect-assisted nonradiative recombination rates in halide perovskites from first principles, the use of semilocal exchange-correlation functionals and the neglect of the SOC effect severely affect the accuracy of the defect levels (as shown in the literature[62,129]) and thus the corresponding recombination rates. Detailed studies of relevant defects and quantitative evaluation of their recombination rates using an accurate hybrid functional with the SOC effect properly included are called for.

We showed that Auger recombination limits efficiency at high carrier densities and can be

detrimental for light emitters. Fortunately, band-structure engineering can be effective in suppressing Auger: we discussed the chemical trends derived from the electronic structure of different halide perovskites and their impact on Auger recombination. Systematic quantitative studies of the Auger recombination rates and mechanisms for a series of halide perovskites with different chemical compositions would be valuable. Such calculations have not yet been performed due to the fact that computations of Auger recombination are extremely demanding. We hope that further improvements in computational approaches will facilitate such calculations, which will allow accurate assessments of the various materials combinations that are being pursued in the quest for enhanced performance of halide-perovskite optoelectronic devices.

Acknowledgments

This work was supported by the U. S. Department of Energy, Office of Science, Basic Energy Sciences, under Award No. DE-SC0010689. Computational resources were provided by the National Energy Research Scientific Computing Center, a DOE Office of Science User Facility supported by the Office of Science of the U. S. Department of Energy under Contract No. DE-AC0205CH11231.

Received: ((will be filled in by the editorial staff))
Revised: ((will be filled in by the editorial staff))
Published online: ((will be filled in by the editorial staff))

References

[1] D. B. Mitzi, C. A. Feild, Z. Schlesinger, R. B. Laibowitz, *J. Solid State Chem.* **1995**, *114*, 159.

[2] T. Baikie, Y. Fang, J. M. Kadro, M. Schreyer, F. Wei, S. G. Mhaisalkar, M. Graetzel, T. J. White, *J. Mater. Chem. A* **2013**, *1*, 5628.

[3] Chr. Kn. Møller, *Nature* **1957**, *180*, 981.

[4] Chr. Kn. Møller, *Nature* **1958**, *182*, 1436.

[5] A. Kojima, K. Teshima, Y. Shirai, T. Miyasaka, *J Am Chem Soc* **2009**, *131*, 6050.

[6] H.-S. Kim, C.-R. Lee, J.-H. Im, K.-B. Lee, T. Moehl, A. Marchioro, S.-J. Moon, R. Humphry-Baker, J.-H. Yum, J. E. Moser, M. Grätzel, N.-G. Park, *Sci. Rep.* **2012**, *2*, 591.

[7] M. M. Lee, J. Teuscher, T. Miyasaka, T. N. Murakami, H. J. Snaith, *Science* **2012**, *338*, 643.

[8] G. E. Eperon, V. M. Burlakov, P. Docampo, A. Goriely, H. J. Snaith, *Adv. Funct. Mater.* **2014**, *24*, 151.

[9] W. S. Yang, J. H. Noh, N. J. Jeon, Y. C. Kim, S. Ryu, J. Seo, S. I. Seok, *Science* **2015**, *348*, 1234.

[10] M. Saliba, S. Orlandi, T. Matsui, S. Aghazada, M. Cavazzini, J.-P. Correa-Baena, P. Gao, R. Scopelliti, E. Mosconi, K.-H. Dahmen, F. De Angelis, A. Abate, A. Hagfeldt, G. Pozzi, M. Graetzel, M. K. Nazeeruddin, *Nat. Energy* **2016**, *1*, 15017.

[11] M. Saliba, T. Matsui, J.-Y. Seo, K. Domanski, J.-P. Correa-Baena, M. K. Nazeeruddin, S. M. Zakeeruddin, W. Tress, A. Abate, A. Hagfeldt, M. Grätzel, *Energy Env. Sci* **2016**, *9*, 1989.

[12] W. S. Yang, B. Park, E. H. Jung, N. J. Jeon, Y. C. Kim, D. U. Lee, S. S. Shin, J. Seo, E. K. Kim, J. H. Noh, S. I. Seok, *Science* **2017**, *356*, 1376.

[13] M. Kim, G.-H. Kim, T. K. Lee, I. W. Choi, H. W. Choi, Y. Jo, Y. J. Yoon, J. W. Kim, J. Lee, D. Huh, H. Lee, S. K. Kwak, J. Y. Kim, D. S. Kim, *Joule* **2019**, S2542435119303058.

[14] F. Di Giacomo, A. Fakharuddin, R. Jose, T. M. Brown, *Energy Environ. Sci.* **2016**, *9*, 3007.

[15] Y. Zhou, Y. Zhao, *Energy Environ. Sci.* **2019**, *12*, 1495.

[16] M. Lyu, J.-H. Yun, P. Chen, M. Hao, L. Wang, *Adv. Energy Mater.* **2017**, *7*, 1602512.

[17] M. I. Asghar, J. Zhang, H. Wang, P. D. Lund, *Renew. Sustain. Energy Rev.* **2017**, *77*, 131.

[18] T. A. Berhe, W.-N. Su, C.-H. Chen, C.-J. Pan, J.-H. Cheng, H.-M. Chen, M.-C. Tsai, L.-Y. Chen, A. A. Dubale, B.-J. Hwang, *Energy Environ. Sci.* **2016**, *9*, 323.

[19] J. S. Manser, M. I. Saidaminov, J. A. Christians, O. M. Bakr, P. V. Kamat, *Acc. Chem. Res.* **2016**, *49*, 330.

[20] T. Leijtens, G. E. Eperon, N. K. Noel, S. N. Habisreutinger, A. Petrozza, H. J. Snaith, *Adv. Energy Mater.* **2015**, *5*, 1500963.

[21] G. Niu, X. Guo, L. Wang, *J. Mater. Chem. A* **2015**, *3*, 8970.

[22] A. Babayigit, A. Ethirajan, M. Muller, B. Conings, *Nat. Mater.* **2016**, *15*, 247.

[23] Z.-K. Tan, R. S. Moghaddam, M. L. Lai, P. Docampo, R. Higler, F. Deschler, M. Price, A. Sadhanala, L. M. Pazos, D. Credgington, F. Hanusch, T. Bein, H. J. Snaith, R. H. Friend, *Nat. Nanotechnol.* **2014**, *9*, 687.

[24] Q. Zhang, S. T. Ha, X. Liu, T. C. Sum, Q. Xiong, *Nano Lett.* **2014**, *14*, 5995.

[25] J. Luo, J.-H. Im, M. T. Mayer, M. Schreier, M. K. Nazeeruddin, N.-G. Park, S. D. Tilley, H. J. Fan, M. Gratzel, *Science* **2014**, *345*, 1593.

[26] B. Chen, T. Li, Q. Dong, E. Mosconi, J. Song, Z. Chen, Y. Deng, Y. Liu, S. Ducharme, A. Gruverman, F. D. Angelis, J. Huang, *Nat. Mater.* **2018**, *17*, 1020.

[27] Q. Chen, J. Wu, X. Ou, B. Huang, J. Almutlaq, A. A. Zhumekenov, X. Guan, S. Han, L. Liang, Z. Yi, J. Li, X. Xie, Y. Wang, Y. Li, D. Fan, D. B. L. Teh, A. H. All, O. F. Mohammed, O. M. Bakr, T. Wu, M. Bettinelli, H. Yang, W. Huang, X. Liu, *Nature* **2018**, *561*, 88.

[28] J. M. Frost, K. T. Butler, F. Brivio, C. H. Hendon, M. van Schilfgaarde, A. Walsh, *Nano Lett* **2014**, *14*, 2584.

[29] Y. Kutes, L. Ye, Y. Zhou, S. Pang, B. D. Huey, N. P. Padture, *J Phys Chem Lett* **2014**, *5*, 3335.

[30] S. Liu, F. Zheng, N. Z. Koocher, H. Takenaka, F. Wang, A. M. Rappe, *J Phys Chem Lett* **2015**, *6*, 693.

[31] F. Zheng, L. Z. Tan, S. Liu, A. M. Rappe, *Nano Lett* **2015**, *15*, 7794.

[32] X.-Y. Zhu, V. Podzorov, *J Phys Chem Lett* **2015**, *6*, 4758.

[33] E. M. Hutter, M. C. Gélvez-Rueda, A. Osherov, V. Bulović, F. C. Grozema, S. D. Stranks, T. J. Savenije, *Nat Mater* **2016**, *16*, 115.

[34] T. Etienne, E. Mosconi, F. De Angelis, *J Phys Chem Lett* **2016**, *7*, 1638.

[35] L. M. Pazos-Outon, M. Szumilo, R. Lamboll, J. M. Richter, M. Crespo-Quesada, M. Abdi-Jalebi, H. J. Beeson, M. Vru ini, M. Alsari, H. J. Snaith, B. Ehrler, R. H. Friend, F. Deschler, *Science* **2016**, *351*, 1430.

[36] Y. Chen, H. T. Yi, X. Wu, R. Haroldson, Y. N. Gartstein, Y. I. Rodionov, K. S. Tikhonov, A. Zakhidov, X.-Y. Zhu, V. Podzorov, *Nat Commun* **2016**, *7*, 12253.

[37] H. Zhu, K. Miyata, Y. Fu, J. Wang, P. P. Joshi, D. Niesner, K. W. Williams, S. Jin, X.-Y. Zhu, *Science* **2016**, *353*, 1409.

[38] T. Chen, W.-L. Chen, B. J. Foley, J. Lee, J. P. C. Ruff, J. Y. P. Ko, C. M. Brown, L. W. Harriger, D. Zhang, C. Park, M. Yoon, Y.-M. Chang, J. J. Choi, S.-H. Lee, *Proc Natl Acad Sci USA* **2017**, *114*, 7519.

[39] J. Fu, Q. Xu, G. Han, B. Wu, C. H. A. Huan, M. L. Leek, T. C. Sum, *Nat Commun* **2017**, *8*, 1300.

[40] C. Wehrenfennig, G. E. Eperon, M. B. Johnston, H. J. Snaith, L. M. Herz, *Adv Mater* **2014**, *26*, 1584.

[41] Y. Yang, M. Yang, Z. Li, R. Crisp, K. Zhu, M. C. Beard, *J. Phys. Chem. Lett.* **2015**, *6*, 4688.

[42] R. L. Milot, G. E. Eperon, H. J. Snaith, M. B. Johnston, L. M. Herz, *Adv Funct Mater* **2015**, *25*, 6218.

[43] J. M. Richter, M. Abdi-Jalebi, A. Sadhanala, M. Tabachnyk, J. P. H. Rivett, L. M. Pazos-Outón, K. C. Gödel, M. Price, F. Deschler, R. H. Friend, *Nat Commun* **2016**, *7*, 13941.

[44] L. M. Herz, *Annu Rev Phys Chem* **2016**, *67*, 65.

[45] C. Wehrenfennig, M. Liu, H. J. Snaith, M. B. Johnston, L. M. Herz, *Energy Env. Sci* **2014**, *7*, 2269.

[46] T. W. Crothers, R. L. Milot, J. B. Patel, E. S. Parrott, J. Schlipf, P. Müller-Buschbaum, M. B. Johnston, L. M. Herz, *Nano Lett* **2017**, *17*, 5782.

[47] J. Piprek, *Phys. Status Solidi A* **2010**, *207*, 2217.

[48] S. Picozzi, R. Asahi, C. B. Geller, A. J. Freeman, *Phys. Rev. Lett.* **2002**, *89*, 197601.

[49] L. Shi, L.-W. Wang, *Phys. Rev. Lett.* **2012**, *109*, 245501.

[50] A. Alkauskas, Q. Yan, C. G. Van de Walle, *Phys Rev B* **2014**, *90*, 075202.

[51] E. Kioupakis, Q. Yan, D. Steiauf, C. G. Van de Walle, *New J Phys* **2013**, *15*, 125006.

[52] E. Kioupakis, D. Steiauf, P. Rinke, K. T. Delaney, C. G. Van de Walle, *Phys. Rev. B* **2015**, *92*, 035207.

[53] R. Long, J. Liu, O. V. Prezhdo, *J. Am. Chem. Soc.* **2016**, *138*, 3884.

[54] J. Li, H.-F. Zhu, Y.-Y. Zhang, Z.-K. Yuan, S. Chen, X.-G. Gong, *Phys Rev B* **2017**, *96*, 104103.

[55] X. Zhang, J.-X. Shen, C. G. Van de Walle, *J. Phys. Chem. Lett.* **2018**, *9*, 2903.

[56] X. Zhang, J.-X. Shen, W. Wang, C. G. Van de Walle, *ACS Energy Lett.* **2018**, *3*, 2329.

[57] J.-X. Shen, X. Zhang, S. Das, E. Kioupakis, C. G. Van De Walle, *Adv Energy Mater* **2018**, *8*, 1801027.

[58] J. M. Richter, K. Chen, A. Sadhanala, J. Butkus, J. P. H. Rivett, R. H. Friend, B. Monserrat, J. M. Hodgkiss, F. Deschler, *Adv. Mater.* **2018**, 1803379.

[59] C. L. Davies, M. R. Filip, J. B. Patel, T. W. Crothers, C. Verdi, A. D. Wright, R. L. Milot, F. Giustino, M. B. Johnston, L. M. Herz, *Nat Commun* **2018**, *9*, 293.

[60] J. Huang, Y. Yuan, Y. Shao, Y. Yan, *Nat. Rev. Mater.* **2017**, *2*, 17042.

[61] Z. Xiao, Y. Yan, *Adv Energy Mater* **2017**, *7*, 1701136.

[62] D. Meggiolaro, F. De Angelis, *ACS Energy Lett.* **2018**, *3*, 2206.

[63] P. T. Landsberg, *Recombination in Semiconductors*, Cambridge University Press, New York, **1991**.

[64] B. K. Ridley, *Quantum Processes in Semiconductors*, Oxford University Press, New York, **2013**.

[65] G. Kresse, J. Furthmüller, *Phys Rev B* **1996**, *54*, 11169.

[66] P. Giannozzi, S. Baroni, N. Bonini, M. Calandra, R. Car, C. Cavazzoni, D. Ceresoli, G. L. Chiarotti, M. Cococcioni, I. Dabo, A. Dal Corso, S. de Gironcoli, S. Fabris, G. Fratesi, R. Gebauer, U. Gerstmann, C. Gougoussis, A. Kokalj, M. Lazzeri, L. Martin-Samos, N. Marzari, F. Mauri, R. Mazzarello, S. Paolini, A. Pasquarello, L. Paulatto, C. Sbraccia, S. Scandolo, G. Sclauzero, A. P. Seitsonen, A. Smogunov, P. Umari, R. M. Wentzcovitch, *J. Phys. Condens. Matter* **2009**, *21*, 395502.

[67] M. Gajdoš, K. Hummer, G. Kresse, J. Furthmüller, F. Bechstedt, *Phys Rev B* **2006**, *73*, 045112.

[68] N. Marzari, A. A. Mostofi, J. R. Yates, I. Souza, D. Vanderbilt, *Rev Mod Phys* **2012**, *84*, 1419.

[69] G. Cappellini, R. Del Sole, L. Reining, F. Bechstedt, *Phys Rev B* **1993**, *47*, 9892.

[70] T. M. Brenner, D. A. Egger, L. Kronik, G. Hodes, D. Cahen, *Nat Rev Mater* **2016**, *1*, 15007.

[71] P. Azarhoosh, S. McKechnie, J. M. Frost, A. Walsh, M. Van Schilfgaarde, *APL Mater* **2016**, *4*, 091501.

[72] J. Moser, *Nat Mater* **2016**, *16*, 4.

[73] Y. Yamada, T. Nakamura, M. Endo, A. Wakamiya, Y. Kanemitsu, *J Am Chem Soc* **2014**, *136*, 11610.

[74] C. La-o-vorakiat, T. Salim, J. Kadro, M.-T. Khuc, R. Haselsberger, L. Cheng, H. Xia, G. G. Gurzadyan, H. Su, Y. M. Lam, R. A. Marcus, M.-E. Michel-Beyerle, E. E. M. Chia, *Nat. Commun.* **2015**, *6*, 7903.

[75] D. Bi, W. Tress, M. I. Dar, P. Gao, J. Luo, C. Renevier, K. Schenk, A. Abate, F. Giordano, J.-P. Correa Baena, J.-D. Decoppet, S. M. Zakeeruddin, M. K. Nazeeruddin, M. Gra tzel, A. Hagfeldt, *Sci Adv* **2016**, *2*, e1501170.

[76] J. Li, P. M. Haney, *Phys Rev B* **2016**, *93*, 155432.

[77] J. Li, P. M. Haney, *Appl Phys Lett* **2016**, *109*, 193903.

[78] Z.-G. Yu, *Phys Chem Chem Phys* **2017**, *19*, 14907.

[79] T. Kirchartz, U. Rau, *J Phys Chem Lett* **2017**, *8*, 1265.

[80] Yu. A. Bychkov, E. I. Rashba, *JETP Lett* **1984**, *39*, 78.

[81] A. Manchon, H. C. Koo, J. Nitta, S. M. Frolov, R. a Duine, *Nat Mater* **2015**, *14*, 871.

[82] G. Dresselhaus, *Phys Rev* **1955**, *100*, 580.

[83] D. Niesner, M. Wilhelm, I. Levchuk, A. Osvet, S. Shrestha, M. Batentschuk, C. Brabec, T. Fauster, *Phys Rev Lett* **2016**, *117*, 1.

[84] C. Motta, F. El-Mellouhi, S. Kais, N. Tabet, F. Alharbi, S. Sanvito, *Nat Commun* **2015**, *6*, 7026.

[85] A. Stroppa, D. Di Sante, P. Barone, M. Bokdam, G. Kresse, C. Franchini, M.-H. Whangbo, S. Picozzi, *Nat. Commun.* **2014**, *5*, 5900.

[86] A. Stroppa, C. Quarti, F. De Angelis, S. Picozzi, *J Phys Chem Lett* **2015**, *6*, 2223.

[87] J. Heyd, G. E. Scuseria, M. Ernzerhof, *J Chem Phys* **2003**, *118*, 8207.

[88] K. Frohna, T. Deshpande, J. Harter, W. Peng, B. A. Barker, J. B. Neaton, S. G. Louie, O. M. Bakr, D. Hsieh, M. Bernardi, *Nat. Commun.* **2018**, *9*, 1829.

[89] M. Kim, J. Im, A. J. Freeman, J. Ihm, H. Jin, *Proc Natl Acad Sci* **2014**, *111*, 6900.

[90] J. Hader, J. V. Moloney, S. W. Koch, in *Proc SPIE* (Eds.: M. Osinski, F. Henneberger, Y. Arakawa), **2006**, p. 61151T.

[91] W. Tress, *Adv Energy Mater* **2017**, *7*, 1602358.

[92] C. Quarti, E. Mosconi, F. De Angelis, *Chem. Mater.* **2014**, *26*, 6557.

[93] B. Monserrat, *J. Phys. Condens. Matter* **2018**, *30*, 083001.

[94] D. W. deQuilettes, K. Frohna, D. Emin, T. Kirchartz, V. Bulovic, D. S. Ginger, S. D. Stranks, *Chem. Rev.* **2019**, acs. chemrev.9b00169.

[95] D. Emin, *J. Appl. Phys.* **2018**, *123*, 055105.

[96] H.-H. Fang, R. Raissa, M. Abdu-Aguye, S. Adjokatse, G. R. Blake, J. Even, M. A. Loi, *Adv. Funct. Mater.* **2015**, *25*, 2378.

[97] A. Filippetti, P. Delugas, A. Mattoni, *J Phys Chem C* **2014**, *118*, 24843.

[98] E. Kioupakis, P. Rinke, K. T. Delaney, C. G. Van de Walle, *Appl. Phys. Lett.* **2011**, *98*, 161107.

[99] G.-B. Lin, D. Meyaard, J. Cho, E. Fred Schubert, H. Shim, C. Sone, *Appl. Phys. Lett.* **2012**, *100*, 161106.

[100] K. A. Bulashevich, S. Yu. Karpov, *Phys. Status Solidi C* **2008**, *5*, 2066.

[101] I. Almansouri, M. A. Green, A. Ho-Baillie, *J Mater Res* **2016**, *31*, 2197.

[102] Q. Yan, P. Rinke, A. Janotti, M. Scheffler, C. G. Van de Walle, *Phys. Rev. B* **2014**, *90*, 125118.

[103] L. Zhang, W. Geng, C. Tong, X. Chen, T. Cao, M. Chen, *Sci. Rep.* **2018**, *8*, 7760.

[104] M. Szafrański, A. Katrusiak, *J. Phys. Chem. Lett.* **2016**, *7*, 3458.

[105] C. Zhu, X. Niu, Y. Fu, N. Li, C. Hu, Y. Chen, X. He, G. Na, P. Liu, H. Zai, Y. Ge, Y. Lu, X. Ke, Y. Bai, S. Yang, P. Chen, Y. Li, M. Sui, L. Zhang, H. Zhou, Q. Chen, *Nat. Commun.* **2019**, *10*, 815.

[106] R. Prasanna, A. Gold-Parker, T. Leijtens, B. Conings, A. Babayigit, H.-G. Boyen, M. F. Toney, M. D. McGehee, *J. Am. Chem. Soc.* **2017**, *139*, 11117.

[107] G. Liu, L. Kong, W. Yang, H. Mao, *Mater. Today* **2019**, S1369702118309489.

[108] M. B. Johnston, L. M. Herz, *Acc Chem Res* **2016**, *49*, 146.

[109] K. Robinson, G. V. Gibbs, P. H. Ribbe, *Science* **1971**, *172*, 567.

[110] S. Zollner, S. Gopalan, M. Cardona, *J. Appl. Phys.* **1990**, *68*, 1682.

[111] Q. Yan, E. Kioupakis, D. Jena, C. G. Van de Walle, *Phys. Rev. B* **2014**, *90*, 121201.

[112] H. Cho, S.-H. Jeong, M.-H. Park, Y.-H. Kim, C. Wolf, C.-L. Lee, J. H. Heo, A. Sadhanala, N. Myoung, S. Yoo, S. H. Im, R. H. Friend, T.-W. Lee, *Science* **2015**, *350*, 1222.

[113] J. Song, J. Li, X. Li, L. Xu, Y. Dong, H. Zeng, *Adv. Mater.* **2015**, *27*, 7162.

[114] Y.-H. Kim, H. Cho, J. H. Heo, T.-S. Kim, N. Myoung, C.-L. Lee, S. H. Im, T.-W. Lee, *Adv. Mater.* **2015**, *27*, 1248.

[115] J. Wang, N. Wang, Y. Jin, J. Si, Z.-K. Tan, H. Du, L. Cheng, X. Dai, S. Bai, H. He, Z. Ye, M. L. Lai, R. H. Friend, W. Huang, *Adv. Mater.* **2015**, *27*, 2311.

[116] M. Yuan, L. N. Quan, R. Comin, G. Walters, R. Sabatini, O. Voznyy, S. Hoogland, Y. Zhao, E. M. Beauregard, P. Kanjanaboos, Z. Lu, D. H. Kim, E. H. Sargent, *Nat. Nanotechnol.* **2016**, *11*, 872.

[117] N. Wang, L. Cheng, R. Ge, S. Zhang, Y. Miao, W. Zou, C. Yi, Y. Sun, Y. Cao, R. Yang, Y. Wei, Q. Guo, Y. Ke, M. Yu, Y. Jin, Y. Liu, Q. Ding, D. Di, L. Yang, G. Xing, H. Tian, C. Jin, F. Gao, R. H. Friend, J. Wang, W. Huang, *Nat. Photonics* **2016**, *10*, 699.

[118] Y. Ling, Z. Yuan, Y. Tian, X. Wang, J. C. Wang, Y. Xin, K. Hanson, B. Ma, H. Gao, *Adv. Mater.* **2016**, *28*, 305.

[119] J. Byun, H. Cho, C. Wolf, M. Jang, A. Sadhanala, R. H. Friend, H. Yang, T.-W. Lee, *Adv. Mater.* **2016**, *28*, 7515.

[120] J. Pan, L. N. Quan, Y. Zhao, W. Peng, B. Murali, S. P. Sarmah, M. Yuan, L. Sinatra, N. M. Alyami, J. Liu, E. Yassitepe, Z. Yang, O. Voznyy, R. Comin, M. N. Hedhili, O. F. Mohammed, Z. H. Lu, D. H. Kim, E. H. Sargent, O. M. Bakr, *Adv. Mater.* **2016**, *28*, 8718.

[121] L. Zhang, X. Yang, Q. Jiang, P. Wang, Z. Yin, X. Zhang, H. Tan, Y. Yang, M. Wei, B. R. Sutherland, E. H. Sargent, J. You, *Nat. Commun.* **2017**, *8*, 15640.

[122] Z. Xiao, R. A. Kerner, L. Zhao, N. L. Tran, K. M. Lee, T.-W. Koh, G. D. Scholes, B. P. Rand, *Nat. Photonics* **2017**, *11*, 108.

[123] W.-J. Yin, T. Shi, Y. Yan, *Appl Phys Lett* **2014**, *104*, 063903.

[124] J. Kang, L.-W. Wang, *J. Phys. Chem. Lett.* **2017**, *8*, 489.

[125] J. R. Poindexter, R. L. Z. Hoye, L. Nienhaus, R. C. Kurchin, A. E. Morishige, E. E. Looney, A. Osherov, J. P. Correa-Baena, B. Lai, V. Bulović, V. Stevanović, M. G. Bawendi, T. Buonassisi, *ACS Nano* **2017**, *11*, 7101.

[126] J. Wiktor, F. Ambrosio, A. Pasquarello, *J. Mater. Chem. A* **2018**, *6*, 16863.

[127] D. Meggiolaro, S. G. Motti, E. Mosconi, A. J. Barker, J. Ball, C. Andrea Riccardo Perini, F. Deschler, A. Petrozza, F. De Angelis, *Energy Environ. Sci.* **2018**, *11*, 702.

[128] A. Buin, P. Pietsch, J. Xu, O. Voznyy, A. H. Ip, R. Comin, E. H. Sargent, *Nano Lett.* **2014**, *14*, 6281.

[129] M.-H. Du, *J Phys Chem Lett* **2015**, *6*, 1461.

[130] A. Baumann, S. Väth, P. Rieder, M. C. Heiber, K. Tvingstedt, V. Dyakonov, *J. Phys. Chem. Lett.* **2015**, *6*, 2350.

[131] S. Heo, G. Seo, Y. Lee, D. Lee, M. Seol, J. Lee, J.-B. Park, K. Kim, D.-J. Yun, Y. S. Kim, J. K. Shin, T. K. Ahn, M. K. Nazeeruddin, *Energy Environ. Sci.* **2017**, *10*, 1128.

Biographies

Dr. Xie Zhang received his PhD in 2015 from the Department of Computational Materials Design (Dir. Prof. Neugebauer) at the Max-Planck-Institut für Eisenforschung GmbH and Ruhr-Universität Bochum. He continued working on phase transformations in alloys as a postdoc until December 2016. Since joining the group of Prof. Van de Walle at the University of California, Santa Barbara in 2017, he focuses on computing and understanding the fundamental recombination mechanisms in optoelectronic materials from first principles.

Dr. Jimmy-Xuan Shen received his PhD from the Physics Department at the University of California, Santa Barbara under Prof. Van de Walle. His PhD focused on developing methodologies to investigate recombination mechanisms in materials with strong relativistic effects. He joined the group of Prof. Persson at the University of California, Berkeley in 2018 and is currently working on high-throughput computational studies of cathode materials and featurizing of quantum chemistry results for machine-learning applications.

Chris G. Van de Walle is a Distinguished Professor of Materials at the University of California, Santa Barbara. He received his Ph.D. from Stanford University in 1986. Prior to joining UCSB in 2004, he was a Principal Scientist at Xerox PARC. Van de Walle develops and applies computational techniques to study electronic, optical, and vibrational properties of point defects, surfaces, and interfaces. Current interests include novel electronic materials and spin centers for quantum information science.

Table of contents entry:

Recent progress in first-principles simulations of carrier recombination in halide perovskites is reviewed. Misunderstandings relating to the impact of the Rashba effect on radiative recombination are clarified. The origin of exceptionally strong Auger recombination and avenues for improved materials design are discussed. Critical analysis of the recombination mechanisms reveals fruitful directions for improving the performance of halide perovskites.

Keyword: First principles, radiative recombination, Auger recombination, halide perovskites

Xie Zhang*, Jimmy-Xuan Shen*, and Chris G. Van de Walle*

Title First-principles simulation of carrier recombination mechanisms in halide perovskites